



**HAL**  
open science

## Dates and rates of endo-exorheic drainage development: Insights from fluvial terraces (Duero River, Iberian Peninsula)

Laura Rodríguez-Rodríguez, Loreto Antón, Ángel Rodés, Raimon Pallàs,  
Daniel García-Castellanos, Ivone Jiménez-Munt, Lucía Struth, Laëtitia  
Leanni, A.S.T.E.R. Team, Georges Aumaitre, et al.

### ► To cite this version:

Laura Rodríguez-Rodríguez, Loreto Antón, Ángel Rodés, Raimon Pallàs, Daniel García-Castellanos, et al.. Dates and rates of endo-exorheic drainage development: Insights from fluvial terraces (Duero River, Iberian Peninsula). *Global and Planetary Change*, 2020, 193, pp.103271. 10.1016/j.gloplacha.2020.103271 . hal-03153524

**HAL Id: hal-03153524**

**<https://hal.science/hal-03153524>**

Submitted on 22 Aug 2022

**HAL** is a multi-disciplinary open access archive for the deposit and dissemination of scientific research documents, whether they are published or not. The documents may come from teaching and research institutions in France or abroad, or from public or private research centers.

L'archive ouverte pluridisciplinaire **HAL**, est destinée au dépôt et à la diffusion de documents scientifiques de niveau recherche, publiés ou non, émanant des établissements d'enseignement et de recherche français ou étrangers, des laboratoires publics ou privés.



Distributed under a Creative Commons Attribution - NonCommercial 4.0 International License

1 **DATES AND RATES OF ENDO-EXORHEIC DRAINAGE DEVELOPMENT:**  
2 **INSIGHTS FROM FLUVIAL TERRACES (DUERO RIVER, IBERIAN**  
3 **PENINSULA)**

4 **Laura Rodríguez-Rodríguez<sup>1,2\*</sup>, Loreto Antón<sup>3</sup>, Ángel Rodés<sup>4</sup>, Raimon Pallàs<sup>5</sup>,**  
5 **Daniel García-Castellanos<sup>6</sup>, Ivone Jiménez-Munt<sup>6</sup>, Lucía Struth<sup>6</sup>, Laëtítia Leanni<sup>7</sup>,**  
6 **ASTER Team<sup>7</sup>**

7 <sup>1</sup> Departamento de Ciencias de la Tierra y Física de la Materia Condensada,  
8 Universidad de Cantabria, Avenida de los Castros 48, 93005 Santander, Spain.

9 <sup>2</sup> Laboratoire de Géographie Physique (UMR 8591, CNRS), 1 Place Aristide Briand  
10 92195 Meudon, France.

11 <sup>3</sup> Universidad Nacional de Educación a Distancia (UNED), Departamento de Ciencias  
12 Analíticas, Senda del Rey 9, Madrid, Spain.

13 <sup>4</sup> NERC Cosmogenic Isotope Analysis Facility, Scottish Universities Environmental  
14 Research Centre, East Kilbride G75 0QF United Kingdom.

15 <sup>5</sup> Institut de Recerca Geomodels, RISKNAT Group, Departament de Dinàmica de la  
16 Terra i de l'Oceà, Universitat de Barcelona, Martí i Franques s/n, Barcelona, Spain.

17 <sup>6</sup> Institut de Ciències de la Terra Jaume Almera, ICTJA-CSIC, Solé i Sabaris s/n,  
18 Barcelona, Spain.

19 <sup>7</sup>Aix Marseille Université, CNRS, IRD, INRA, Coll France, UM34 CEREGE,  
20 Technopôle de l'Environnement Arbois-Méditerranée, BP80,13545 Aix-en-Provence,  
21 France. [ASTER Team: Georges Aumaître, Didier Bourlès, Karim Keddadouche]

22 \* [laura.rodriquezr@unican.es](mailto:laura.rodriquezr@unican.es) (Corresponding author: L. Rodríguez-Rodríguez)

23        **Abstract**

24    Fluvial terraces are valuable records to study and characterize landscape evolution and  
25    river response to base level lowering, and to decipher coupled responses between fluvial  
26    incision and regional tectonics. The opening of closed basins has a strong impact on  
27    fluvial dynamics, as it involves an abrupt base level lowering that accelerates landscape  
28    fluvial dissection. This study focuses on the time response of the Duero Basin, the  
29    largest and best preserved among the Cenozoic basins of the Iberian Peninsula, to  
30    exorheism. Fluvial incision due to basin opening has developed up to 13 un-paired  
31    strath terraces along the south margin of the Duero river, distributed at relative heights  
32    up to +136–128 m compared to the modern floodplain. Paired  $^{10}\text{Be}$ – $^{26}\text{Al}$  cosmogenic  
33    isotope depth profiles from six fluvial terraces, located ca. 30 to 80 km upstream from  
34    the opening zone, suggest Pleistocene ages for almost the entire fluvial terrace staircase  
35    (from T3 at +112–107 m, to T12 at +13–11 m). The terrace density and the total  
36    lowering of the terrace surface, key parameters in limiting terrace exposure ages, were  
37    estimated based on field and geomorphological data. Apparent burial durations and  
38    basin denudation rates deduced from inherited  $^{10}\text{Be}$ – $^{26}\text{Al}$  concentrations provide  
39    valuable information on basin evolution. Apparent basin denudation rates remained  
40    relatively low ( $<3\text{--}6\text{ m}\cdot\text{Ma}^{-1}$ ) during the Pliocene, and doubled ( $8\text{--}13\text{ m}\cdot\text{Ma}^{-1}$ ) during  
41    the Early Pleistocene (ca. 2–1 Ma) possibly showing a lower proportion of recycled  
42    sediments. Time averaged incision rates deduced from terraces in the study area and  
43    along some tributaries show that incision rates are higher close to the opening site (122  
44    to  $<250\text{ m}\cdot\text{Ma}^{-1}$ ) than towards the upstream part of the catchment ( $88\text{--}68\text{ m}\cdot\text{Ma}^{-1}$ ),  
45    evidencing the retrogressive travel of the erosive wave nucleated at the opening site.

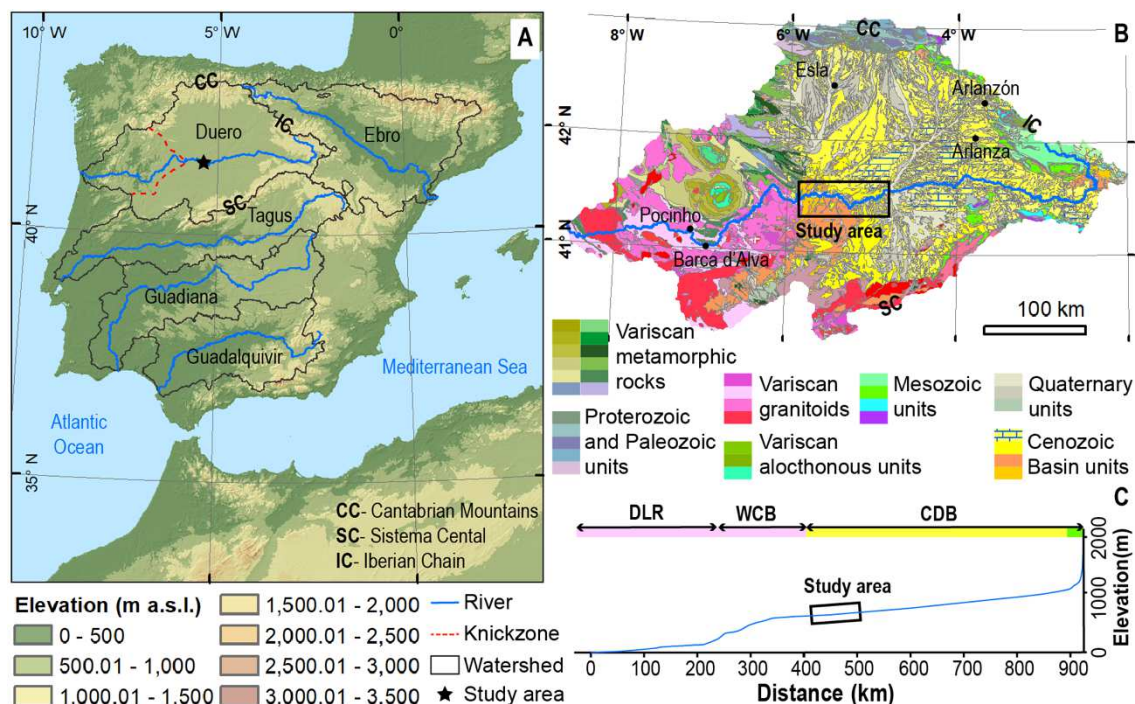
## 46 **1. Introduction**

47 Endorheic basins (also named closed, intermountain, or internally-drained basins)  
48 are depressions lacking any water outflow towards the ocean. They constitute valuable  
49 records for understanding the evolution and dynamics of surface processes on a range of  
50 spatial scales, as they trap sediments until they eventually become externally drained  
51 (exorheic), then excavating and exposing their sedimentary record and forming  
52 planation surfaces and fluvial terraces, which allows deciphering landscape evolution  
53 (García-Castellanos et al., 2003; Yu et al., 2014; He et al., 2017). Investigating how  
54 basins evolve after an endo-exorheic transition is key for understanding long-term  
55 landscape evolution (at geologic timescale) and for elucidating the mechanisms by  
56 which large basins recover a steady state profile. This is most dramatically expressed in  
57 the event of large drainage changes caused by fluvial captures, by sediment/water  
58 overfilling of basins that leads to basin spillover, or by a combination of these  
59 mechanisms (Spencer and Pearthree, 2001; García-Castellanos and Larrasoña, 2015;  
60 Richardson et al., 2008; Heidarzadeh et al., 2017). For example, based on apatite  
61 fission track analysis and stratigraphic sections, Richardson et al. (2008) found that the  
62 Sichuan Basin (central China) underwent accelerated widespread erosion of 1 to 4 km  
63 of overlying sedimentary material after the Yangtze River started excavating the Three  
64 Gorges. Similarly, the Ebro Basin (NE Spain) underwent the excavation of up to a  
65 kilometer of sediment after its endorheic lake system was captured by or spilled over  
66 the Ebro River ca. 8-12 Ma ago (García-Castellanos et al., 2003). Fluvial terrace  
67 architecture is key to understand how fast large basins might respond after an endo-  
68 exorheic transition and which factors control how the wave of incision is transmitted  
69 upstream. The review work of Demoulin et al. (2017) stands out that fluvial terrace  
70 patterns and timing of fluvial incision are essential information to isolate the effects of  
71 other driving factors for erosion that might be also involved in terrace formation such as  
72 tectonics, climate variations, and other non-tectonic factors (such as bedrock lithology).  
73 However, few studies focus on continental-scale drainage reorganization and, within  
74 those, most studies lack rigorous age control to allow accurate insights into erosion rates  
75 and the timing of large-scale landscape modification.

76 The Iberian Peninsula is known for the occurrence of several large-scale foreland  
77 basins formed during the Alpine Orogeny that evolved as closed basins during a  
78 significant part of the Cenozoic (Friend and Dabrio, 1996). These basins later became  
79 externally drained towards the Atlantic Ocean and the Mediterranean Sea, exposing

80 their infill sequences by fluvial down-cutting in response to basin opening (Figure 1).  
81 Santisteban and Schulte (2007) reviewed fluvial terrace patterns in the major Iberian  
82 basins (Duero, Ebro, Tagus, Guadalquivir and Guadiana) and concluded that the time of  
83 incision and river response to basin opening is highly variable depending on  
84 local/regional climate, glacio-eustatic sea-level changes, and local/regional tectonics.  
85 Hence, while some basins such as the Ebro Basin have suffered remarkable erosion of  
86 their infill sequence (García-Castellanos and Larrasoña, 2015), others remain relatively  
87 intact. For example, the Duero Basin stands a transient river profile since the endo-  
88 exorheic transition (Antón et al., 2012, 2014; Figure 1), recording scarce total  
89 denudation due to fluvial entrenchment caused by base level lowering (Antón et al.,  
90 2019). A cross comparison between the morphometric indices and knickpoint  
91 distribution in the Ebro and Duero basins suggests a short-term aggressive role of the  
92 Ebro network (responsible for the westward migration observed in the water divide that  
93 separates both basins), but a large-scale aggressor role for the Duero over the Ebro in  
94 the long-term based on chi-analysis (Struth et al., 2019). Particularly, the Duero river  
95 displays two trains of knickpoints that propagate differently through the soft Cenozoic  
96 sediment cover and the Paleozoic crystalline bedrock (Struth et al., 2019), consistently  
97 with the few incision rates available in the Arlanzón and Esla tributaries (Moreno et al.,  
98 2012; Schaller et al., 2016a). Either a younger opening age for the Duero Basin  
99 compared to other Iberian basins (> 3 Ma according to Antón et al., 2019; ~3.7–1.8 Ma  
100 according to Cunha et al., 2019; 1.1–1.9 Ma according to Silva et al., 2017) and/or the  
101 resistant lithology that configures the Duero basin fringe (Struth et al., 2019) could  
102 explain the differences observed in fluvial entrenchment in response to sudden base-  
103 level lowering caused by an endo-exorheic transition. Here, we target a sequence of  
104 thirteen inset fluvial strath terraces formed in response to the Duero endo-exorheic  
105 transition, which are now hanging at heights up to +136–128 m above the modern  
106 floodplain (Rodríguez-Rodríguez et al., 2020; Figure 2). The sequence is preserved at  
107 the western end of the Cenozoic Duero Basin (CDB), along the 90 km-long reach  
108 placed ca. 30 km upstream from the major Arribes knickzone (Figure 1). The Arribes  
109 knickzone is excavated in the Paleozoic crystalline bedrock, along the WCB (Western  
110 fringe of the Cenozoic Basin) which separates the Duero Lower Reach (DLR) from the  
111 Cenozoic sedimentary infill of the CDB (Antón et al. 2012; Figure 1). We fitted the  
112 Combined Surface Exposure-Burial Dating (CSEB) model to our  $^{10}\text{Be}$  and  $^{26}\text{Al}$  depth-  
113 profile data in order to produce a numerical geochronology of six terraces belonging to

114 the Duero fluvial staircase, allowing us to discuss: (i) terrace depositional ages; (ii)  
 115 changes in denudation rates at basin scale over time; (iii) fluvial incision rates in  
 116 response to base level lowering and fluvial entrenchment, and (iv) discuss the upstream  
 117 transmission of the erosion wave caused by the endo-exorheic transition.



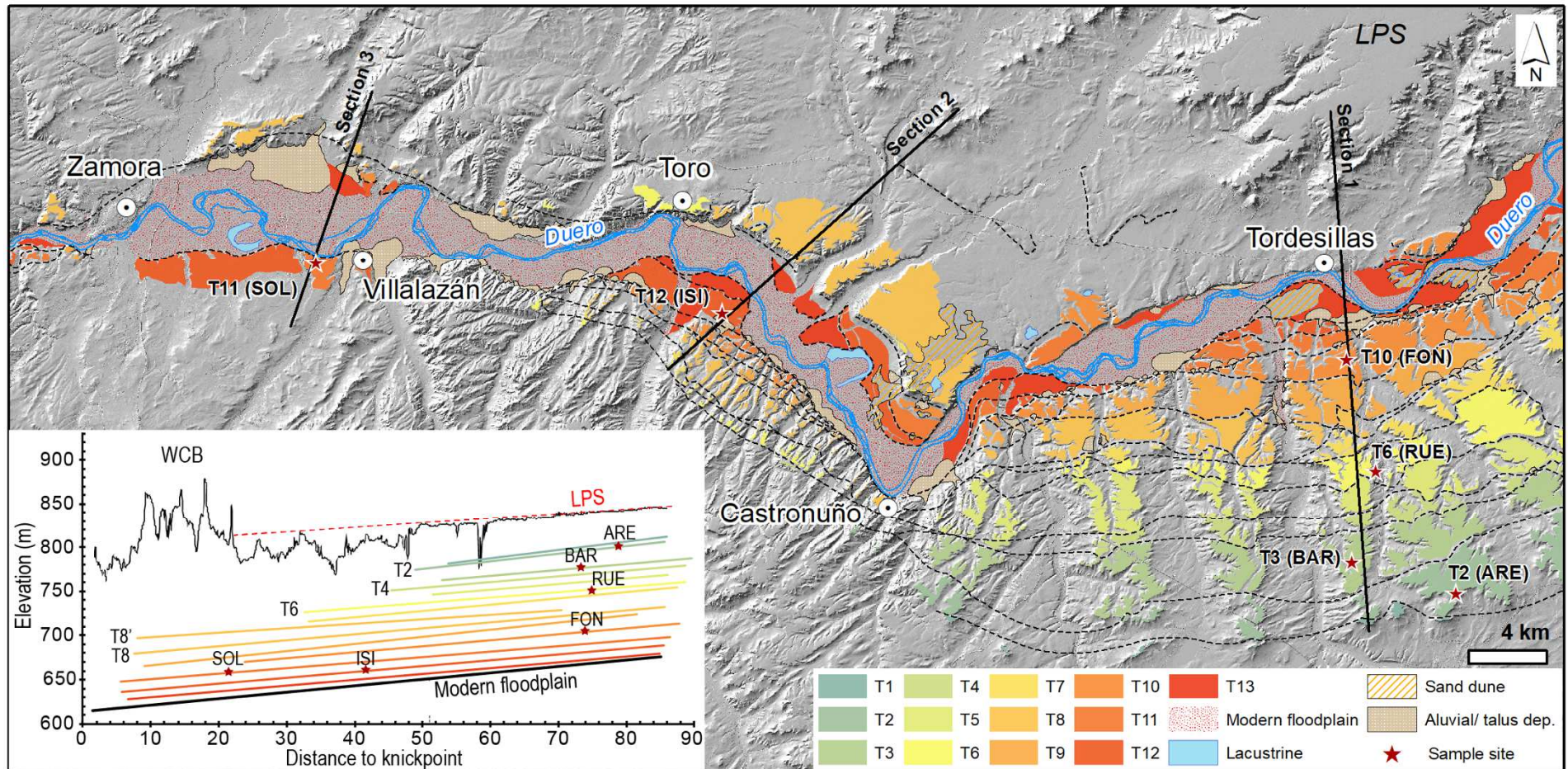
118  
 119 Figure 1.- The Cenozoic Duero Basin (CDB) is the largest Iberian basin that best-  
 120 preserves both the pre-opening topography and the endorheic sedimentary infill  
 121 sequence (Antón et al., 2012, 2019). The CDB is limited by the Cantabrian Mountains  
 122 to the north, the Iberian Chain to the east, the Sistema Central to the south, and the  
 123 Western fringe of the Cenozoic Basin to the west (WCB). The transient long-profile of  
 124 the Duero river shows a knickzone along the WCB (excavated in the Paleozoic  
 125 crystalline bedrock), which separates the Duero Lower Reach (DLR) from the Cenozoic  
 126 sedimentary infill of the CDB (mostly composed by alluvial detrital conglomerate and  
 127 sandstone capped by lacustrine carbonate and evaporitic units). Geologic map source:  
 128 [http://mapas.igme.es/gis/rest/services/Cartografia\\_Geologica/IGME\\_EP\\_Geologico\\_1](http://mapas.igme.es/gis/rest/services/Cartografia_Geologica/IGME_EP_Geologico_1)  
 129 M\_2018/MapServer (last accessed on April 2020).

## 130 2. Geologic and geomorphologic background of the study area

131 The Duero Basin is the largest among the Iberian Cenozoic basins: ~50000 km<sup>2</sup> in  
 132 sediment-covered area and 90400 km<sup>2</sup> in total catchment area (Antón et al., 2019). It  
 133 acted as foreland basin for the Cantabrian Mountains during the Eocene (Alonso et al.,  
 134 1996) and for the Sistema Central between the Oligocene and Miocene (Capote et al.,  
 135 2002), accumulating as much as 3 km of sediments (Gómez-Ortiz et al., 2005). The

136 youngest geologic formation sedimented in endorheic conditions, named the Páramo  
137 Formation, is mostly composed by extensive carbonate facies (mostly limestone, marl  
138 and gypsum) that suggests major expansion of lake environments at the basin's  
139 depocenter during the middle and upper Miocene (Alonso-Zarza et al., 2002). Based on  
140 magnetostratigraphic analysis, the top of the Páramo Formation was assigned a  
141 Tortonian age (9.7–9.6 Ma according to Krijgsman et al., 1996; ~9.1 Ma according to  
142 Beamoud et al., 2006). In contrast, mammal assemblages found at the youngest  
143 carbonate unit of this formation (the Upper Páramo Limestone, or UPL) yielded  
144 Vallesian ages in the southwest part of the basin (where the record is less complete),  
145 while Turolian ages have been reported for fluvial deposits near the base of the  
146 sequence at the basin center, which might point to a Pliocene age for the top of the UPL  
147 (Alonso-Gavilan et al., 1989; Mediavilla and Dabrio, 1989; Alonso-Zarza et al., 2002  
148 and references therein). However, Santisteban et al. (1997) have interpreted these  
149 fluvial deposits as related to the first stages of fluvial dissection already in exorheic  
150 conditions. A detailed analysis of erosion surfaces in the eastern sector of the basin  
151 (Sierra de Atapuerca in the Iberian Chain) reveals up to four erosional surfaces, the  
152 youngest formed after the Duero Basin opened to the Atlantic (Benito-Calvo and Pérez-  
153 González, 2007). It laterally connects with the Lower Páramo Surface (LPS in Figure  
154 2), developed on top of the Lower Páramo Limestone unit (or LPL) due to differential  
155 exposure in response to fluvial dissection after the basin opening during the Pliocene-  
156 Pleistocene (Benito-Calvo and Pérez-González, 2007). An opening age of ~1.1 to 1.9  
157 Ma has been proposed based on a cross-comparison between the fluvial terrace  
158 staircases preserved in the Duero and the Tagus basins, henceforth attributing the full  
159 sequence of fluvial terraces to the Pleistocene (Silva et al., 2017). However, the age-  
160 height transfer curve reported for the Duero river in their work was supported on the  
161 few numerical ages available for the Arlanzón tributary, close to the source area of  
162 sediments in the Iberian Chain (Figure 1). Finally, an older opening age range of ~3.7–  
163 1.8 Ma has been recently reported based on an extrapolation of incision rates derived  
164 from strath terraces hanging at +53–48 m (360–>230 ka), +34–27 m (57 ka) and +17–  
165 13 m (39–12 ka) between Pocinho and Barca d'Alva (Cunha et al., 2019), downstream  
166 of the Arribes knickzone, in the upper end of the Duero Lower Reach (DLR; Figure 1).





167

168

169

170

171

Figure 2.- Geomorphological map of the fluvial terrace staircase developed by the Duero River upstream the Arribes knickpoint. Terrace sample site locations are shown both in the map and along the reconstructed former river profiles based on statistical analysis of terrace surface points extracted from a high-resolution digital elevation model (Rodríguez-Rodríguez et al., 2020). The swath profile of maximum elevation shows the topographic signature of the LPS erosional surface, presumably linked to the initial emptying of the basin after the endo-exorheic transition.



172 Although the precise location of the opening point for the CDB drainage is  
173 unknown, there is a general consensus about its location at the WCB (Silva et al., 2017  
174 and references therein; Figure 1). This work refers to an opening area located at the  
175 Arribes knickzone (ca. 20-50 km downstream from Zamora; Figure 2) where resistant  
176 bedrock, composed by igneous and metamorphic rocks, controls the initiation and  
177 progression of the continental scale drainage reorganization at the uppermost CDB (e.g.  
178 Struth et al., 2019). The study area covers the lowermost 90 km-long reach of the upper  
179 Duero river placed immediately upstream the Arribes knickzone, in the Spanish regions  
180 of Valladolid and Zamora. Modern climate is characterized by mean annual  
181 precipitation of 366–478 mm (<https://sig.mapama.gob.es/siga/>, accessed on August  
182 2019), with a marked dry season in summer. Mean annual temperature is ~12 °C,  
183 annually displaying less than 49 days of winter temperatures equal or below 0°C (mean  
184 temperature minima values in January are 2.5–5°C) and reaching maxima temperature  
185 values in the range 22.5–25°C during the summer season  
186 ([http://www.aemet.es/es/serviciosclimaticos/datosclimatologicos/atlas\\_climatico/visor\\_](http://www.aemet.es/es/serviciosclimaticos/datosclimatologicos/atlas_climatico/visor_atlas_climatico#enlaces_asociados)  
187 [atlas\\_climatico#enlaces\\_asociados](http://www.aemet.es/es/serviciosclimaticos/datosclimatologicos/atlas_climatico/visor_atlas_climatico#enlaces_asociados), last accessed on April 2020). Fluvial terraces crop  
188 out as un-paired strath terraces formed by incision of the Duero River in the endorheic  
189 infill sequence in response to the base level lowering linked to the endo-exorheic  
190 transition, forming successive bedrock stairs capped with fluvial sediments up to 2–7 m  
191 thick. The elevation difference between the LPS (preserved in the north margin of the  
192 river) and the modern floodplain suggests that total incision overcomes 180 m (Figure  
193 2). Fluvial terraces are preferentially preserved along the south margin of the river,  
194 extending as far as 18 km south from the modern channel and hanging above the  
195 modern floodplain at relative heights of: +136–128 m (T1); +130–124 m (T2); +110–  
196 109 m (T3); +104–101 m (T4); +95–91 m (T5); +88–81 m (T6); c. +77 m (T7); +79–59  
197 m (T8’); +60–55 m (T8); +51–44 m (T9); +40–35 m (T10); +30–10 m (T11); +18–12 m  
198 (T12); and +9–3 m (T13; Rodríguez-Rodríguez et al., 2020). The staircase sequence is  
199 fully represented in the eastern half of the study area, east of Castronuño village, while  
200 only the intermediate and lowest terrace levels are present between Castronuño and the  
201 Arribes knickzone. This pattern is possibly related to the occurrence of higher incision  
202 rates close to the opening site than those recorded upstream over the time period when  
203 terraces T1 to T9 were being deposited. This would explain the more extensive terrace  
204 remnants and the higher number of terrace levels upstream Castronuño than between  
205 Castronuño and the Arribes knickzone. Fluvial long-profiles reconstructed through

206 statistical analysis of terrace surface points extracted from high resolution LiDAR  
207 digital elevation models revealed upstream diverging patterns in the highest terraces,  
208 and downstream diverging to parallel patterns in the intermediate and lowest terrace  
209 levels (Figure 2; Rodríguez-Rodríguez et al., 2020).

### 210 **3. Methodology**

211 The cosmogenic nuclide dating technique applied to sediment landforms relies on  
212 the measurement of various cosmogenic nuclides produced and stored inside the lattice  
213 of a target mineral by the interactions with the cosmic rays (Gosse and Phillips, 2001).  
214 The pair of cosmogenic nuclides most frequently used to study alluvial landforms is  
215  $^{10}\text{Be}$ - $^{26}\text{Al}$ , as they are produced in the same target mineral (quartz) at a ratio of  $\sim 6.75$   
216 largely independent from altitude and latitude (Dunai, 2010). Once sediments are buried  
217 deep enough to be fully shielded from cosmic radiation, their initial concentrations start  
218 to decay at a pace of  $4.9975 \times 10^{-7} \text{ a}^{-1}$  for  $^{10}\text{Be}$  (Chmeleff et al., 2010) and  $9.83 \times 10^{-7} \text{ a}^{-1}$   
219 for  $^{26}\text{Al}$  (Nishiizumi, 2004). If sediments have been sufficiently exposed before being  
220 buried, the residual concentration of paired  $^{10}\text{Be}$ - $^{26}\text{Al}$  cosmogenic nuclides measured in  
221 deep samples can be used to solve for the burial time (Granger and Muzikar, 2001).

222 In this study, the timing of river incision and fluvial terrace formation was  
223 constrained through the CSEB model proposed by Rodés et al. (2014), which considers  
224 the possible occurrence of complex exposure-burial histories before the final deposition  
225 of sediments takes place. It is expressed as function of: (i) the apparent pre-depositional  
226 average exhumation rate at the catchment source area; (ii) the apparent pre-depositional  
227 burial time; (iii) the local denudation rate; and (iv) the terrace surface age.

228 Exhumation rates are considered apparent because, although most reworking  
229 processes change the  $^{10}\text{Be}$ - $^{26}\text{Al}$  signature towards concentrations that suggest lower  
230 erosion rates, there could be scenarios where sediments have been recycled after a long  
231 period of burial and, hence, the  $^{10}\text{Be}$ - $^{26}\text{Al}$  signature would solely reflect the last erosion  
232 rate. In any case, the  $^{10}\text{Be}$ - $^{26}\text{Al}$  signatures shall reflect an apparent erosion rate and an  
233 apparent burial duration, both corresponding to an unbalanced average of all erosion  
234 stages occurred and their respective durations.

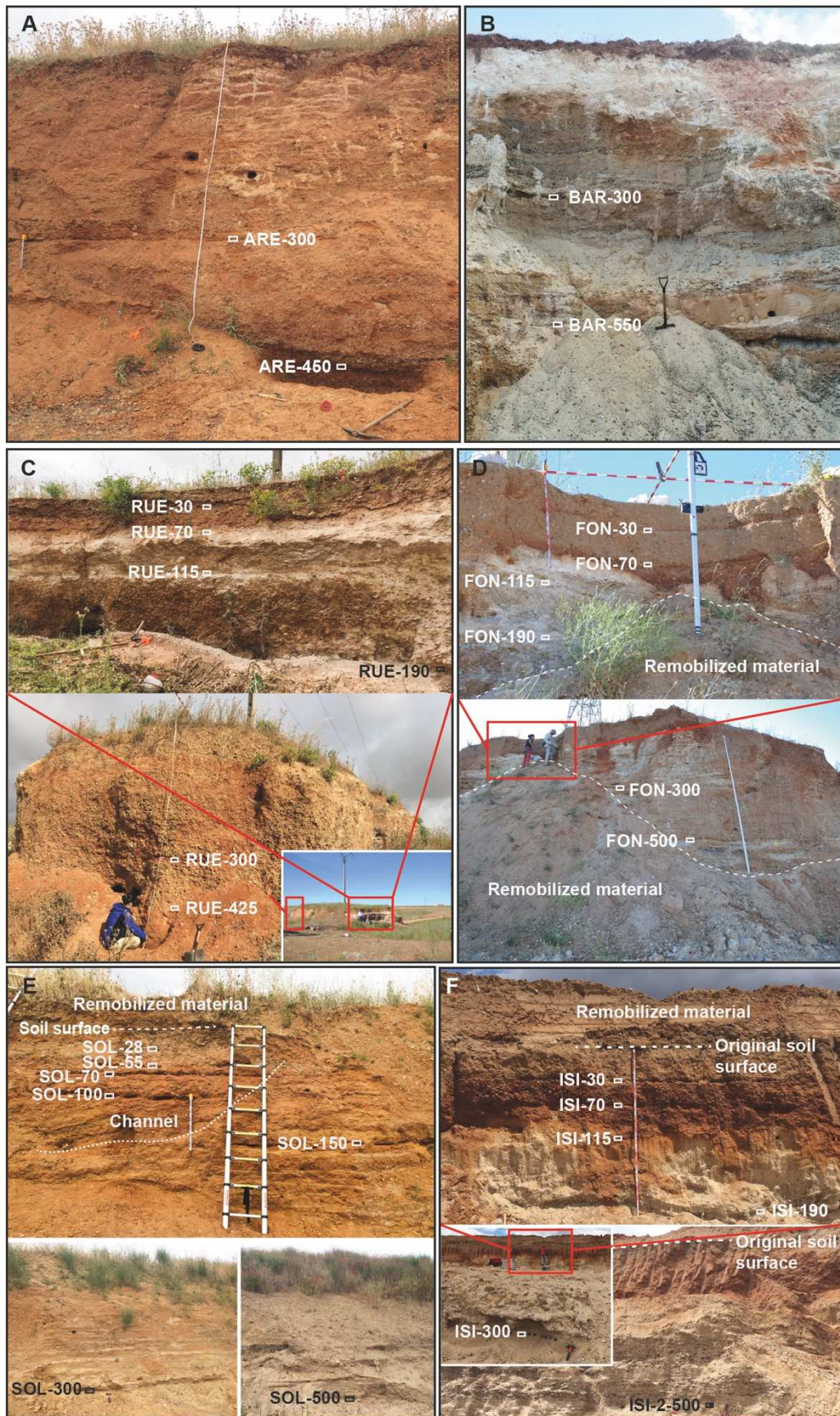
#### 235 *3.1. Terrace depth profile sampling*

236 In order to constrain as much as possible the age of the Duero river terrace staircase,  
237 the thickest terrace sequences, displaying well-preserved top surfaces, were  
238 preferentially targeted for deep profile sampling. We tried to cover the greatest number  
239 of terrace levels distributed over the central CDB, across sections 1, 2, and 3 (located

240 ca. 30-80 km eastward from the WCB; Figure 2). Potential terrace sections were located  
241 using high-resolution LiDAR digital elevation models and aerial imagery  
242 (<https://www.cnig.es>; last access on June 2016), and visited in the field to verify that  
243 sediment thickness was greater than 4 m. Paired  $^{10}\text{Be}$ – $^{26}\text{Al}$  cosmogenic nuclides depth  
244 profiles were sampled from sections of six fluvial terraces of the Duero river staircase,  
245 including a total number of 31 sediment samples taken mostly from sections at open  
246 cast quarries dedicated to gravel extraction (named Arentis, Barbado Martín, Foncantín,  
247 Jose Isidro Torres, and Sola e Hijos). The following terrace levels were sampled  
248 (Figures 2 and 3): T2 (code ARE; 2 samples), T3 (code BAR; 3 samples), T6 (code  
249 RUE; 6 samples), T10 (code FON; 6 samples), T11 (code SOL; 7 samples), and T12  
250 (code ISI; 6 samples). We collected 6–7 sediment samples per terrace profile  
251 exponentially spaced from 20–30 cm below the surface down to 4.25–5 m (Figure 4 and  
252 Table I). In the oldest terraces (T2 and T3), the probability of finding saturated profiles  
253 was considered to be high and, hence, only the deepest samples of the profile (at 3 and  
254 4.50–5.50 m depth, respectively) were taken. The geographic location and altitude of  
255 each sampling site was determined in the field by GPS positioning. The maximum  
256 surface lowering of sampled terrace remnants was inferred using topographic sections  
257 passing through each sampling site, assuming that terrace top surfaces were originally  
258 flat. For this purpose, a 3 m cell-size resolution digital elevation model derived from the  
259 LiDAR datasets from the Spanish National Institute of Geography was used. Fluvial  
260 sediment facies were described at each sampling location. A description of the main soil  
261 characteristics (number of horizons, thickness, presence of pedogenic calcrete) is also  
262 provided to address age interpretations (in terms of possible hiatuses during terrace  
263 aggradation), and to offer an alternative surface lowering scenario for the sampled  
264 terraces. Regarding the grain size fraction sampled, given that fluvial deposits in this  
265 area are cobble- and pebble-dominated, the pebble fraction in the range 2 mm–2 cm in  
266 diameter was targeted in all cases, ensuring that more than 200 particles per sample  
267 were collected.

268 Density values assigned to fluvial sediments might have a strong impact in the final  
269 age model (Rodés et al., 2011). Thus, twenty-three density measurements were  
270 performed in the field for the various fluvial terrace materials identified and sampled,  
271 obtaining results in the range 1.49–2.31  $\text{g}\cdot\text{cm}^{-3}$ , and an average density value of  $1.72 \pm$   
272  $0.2 \text{ g}\cdot\text{cm}^{-3}$  (further details are provided in the supplementary material). Based on these  
273 results, a range of density values of 1.52–1.92  $\text{g}\cdot\text{cm}^{-3}$  has been introduced in the models,

274 which is in good agreement with reference density values provided for dense coarse  
 275 granular soils in some engineering manuals (e.g. González de Vallejo, 2002).



276



277 Figure 3.- Terrace sampling sections: A) T2 at Arentis quarry; B) T3 at Barbado Martín quarry; C)  
278 T6 at an old extraction area close to Rueda; D) T10 at Foncastin quarry; E) T11 at Sola e Hijos quarry;  
279 and F) T12 at Isidro quarry. Labels indicate sampling depths expressed in centimeters.

### 280 3.2. Sample treatment and AMS measurement of Be and Al ratios

281 Fluvial sediment samples were crushed and sieved at the *Departament de Dinàmica*  
282 *de la Terra i de l'Oceà (Universitat de Barcelona)* in order to reduce the grain size to  
283 1mm–250 µm in diameter, optimal for doing the chemical processing. Sample treatment  
284 was conducted at *Laboratoire National des Nucléides Cosmogéniques (LN2C) – Centre*  
285 *Européen de Recherche et d'Enseignement des Géosciences de l'environnement*  
286 (CEREGE, Aix-en-Provence). The extraction of magnetic dark mineral grains was done  
287 using a Frantz magnetic separator and applying a magnetic field intensity of 1A. Sample  
288 cleaning involved carbonate removal with hydrochloric acid and several acid leaching  
289 baths with a mixture of hydrochloric and hexafluorosilicic acids. The isolation and  
290 purification of quartz was done through four etching bathes with hydrofluoric acid to  
291 ensure a full removal of atmospheric  $^{10}\text{Be}$ . Once cleaned, quartz samples (20–30 g)  
292 were spiked with ~100 mg of a phenakite carrier solution with a concentration of  $3025$   
293  $\pm 9 \mu\text{g}\cdot\text{g}^{-1}$  of  $^9\text{Be}$  before total dissolution in hydrofluoric acid. Samples were aliquoted  
294 for the ICP-OES analysis of the natural  $^{27}\text{Al}$  concentration in the samples. Given the  
295 low natural concentration of  $^{27}\text{Al}$  in the samples (mean value of  $2.03 \pm 0.66$  ppm), a  
296 volume of 750–2100 mg of a commercial VWR Prolabo spike solution with a  $^{27}\text{Al}$   
297 concentration of  $981 \pm 4.91 \mu\text{g}\cdot\text{g}^{-1}$  was added to each sample to ensure a final Al  
298 sample of ~2 mg. Beryllium and aluminum were separated from the solution by  
299 successive column chromatography using anionic (DOWEX 1X8) and cationic  
300 (DOWEX 50WX8) resins. The recovered Be and Al solutions were taken to pH ~8.5 to  
301 precipitate the hydroxides, that were subsequently washed in slightly basic solutions.  
302 After drying the last precipitates in porcelain crucibles, samples were heated in the oven  
303 at 800°C during one hour. Resultant BeO and Al<sub>2</sub>O<sub>3</sub> precipitates were mixed with  
304 niobium and silver powder to perform the AMS measurements at the French AMS  
305 National Facility ASTERisques, located at CEREGE (Aix-en-Provence). Beryllium  
306 measurements were calibrated against the reference material NIST–SRM4325 [nominal  
307 value of  $(2.79 \pm 0.03) \times 10^{-11}$  equivalent to 07KNSTD within rounding error], while  
308 aluminum measurements were calibrated against the in-house standard SM-Al-11  
309 [nominal value of  $(7.401 \pm 0.064) \times 10^{-12}$ ] (Arnold et al., 2010). The ASTER  $^{26}\text{Al}$   
310 standard (the only available  $^{26}\text{Al}$  standard cross-calibrated against the primary standards



311 certified by a round-robin exercise) yields a ratio of  $(7.554 \pm 0.104) \times 10^{-12}$  when  
312 measured against the  $^{26}\text{Al}$  KNSTD10650 standard, 2.1% higher than the nominal value  
313 (Rixhon et al., 2011). The SM-Al-11/07KNSTD standardization used in this work  
314 implies a  $^{26}\text{Al}/^{10}\text{Be}$  production ratio of  $6.61 \pm 0.52$  (Braucher et al., 2011), which is in  
315 good agreement with the  $\sim 6.75$  ratio broadly accepted in the literature (Dunai, 2010).  
316 Reported analytical uncertainty ( $1 \sigma$ ) includes: (i) an external uncertainty of  $\sim 0.5\%$  that  
317 accounts for all effects contributing to ASTER's variability (Arnold et al., 2010); (ii) a  
318 counting statistics uncertainty of  $\sim 3\%$  ( $\sim 1,500$  events) related to the cumulative number  
319 of  $^{10}\text{Be}$  events and  $\sim 4\%$  ( $\sim 850$  events) related to the number of  $^{26}\text{Al}$  events acquired  
320 during AMS measurements; and (iii) the uncertainty linked to the chemical blank  
321 correction. The reported analytical uncertainty of the aluminum concentrations also  
322 accounts for the errors associated with the ICP-OES analysis (model Thermo iCAP  
323 5000 Series) carried out at CEREGE. Long-term AMS measurements of procedural  
324 blanks yield a background ratio of  $(2.4 \pm 1.5) \times 10^{-15}$  for  $^{10}\text{Be}/^9\text{Be}$  and  $(2.2 \pm 2.0) \times 10^{-15}$   
325 for  $^{26}\text{Al}/^{27}\text{Al}$  (Bourlès, personal communication). However, the procedural blank in our  
326 dataset yielded ratios of  $3.13 \times 10^{-14}$  for  $^{10}\text{Be}/^9\text{Be}$  and  $8.76 \times 10^{-16}$  for  $^{26}\text{Al}/^{27}\text{Al}$ . We  
327 verified that the unusually high  $^{10}\text{Be}/^9\text{Be}$  ratio observed in the blank responds to a  $^{10}\text{Be}$   
328 contamination of the  $^{27}\text{Al}$  carrier solution ( $\sim 3.507 \times 10^{-12}$  ppm of  $^{10}\text{Be}$ ) that has been  
329 corrected in all samples.

330 Table I.- Location coordinates (in decimal degrees) and terrace top surface elevation at the sampled  
331 terrace depth profiles and measured  $^{10}\text{Be}$  and  $^{26}\text{Al}$  concentrations.

Terrace level	Sample	Depth (cm)	[Be-10] ( $10^3 \text{ at}\cdot\text{g}^{-1}$ )	[Al-26] ( $10^3 \text{ at}\cdot\text{g}^{-1}$ )
T2 41.3522, -4.9159 800 m a.s.l.	ARE-300	$300 \pm 3$	$214.7 \pm 7$	$462 \pm 31$
	ARE-450	$450 \pm 2$	$188.5 \pm 6.1$	$263 \pm 21$
T3 41.3660, -4.9792 779 m a.s.l.	BAR-300	$300 \pm 4$	$340 \pm 12$	$974 \pm 55$
	BAR-550	$550 \pm 3$	$246.5 \pm 8.2$	$302 \pm 22$
	BAR-02-550	$550 \pm 2$	$225 \pm 7.5$	$312 \pm 27$
T6 41.4064, -4.9643 753 m a.s.l.	RUE-030	$30 \pm 2$	$3487 \pm 69$	$15500 \pm 370$
	RUE-070	$70 \pm 2$	$1867 \pm 52$	$5260 \pm 170$
	RUE-115	$115 \pm 2$	$1325 \pm 31$	$4440 \pm 140$
	RUE-190	$190 \pm 3$	$691 \pm 24$	$2102 \pm 75$
	RUE-300	$300 \pm 3$	$436 \pm 14$	$693 \pm 37$
	RUE-425	$425 \pm 2$	$461 \pm 14$	$990 \pm 43$
T10 41.4584, -4.9865 707 m a.s.l.	FON-030	$30 \pm 2$	$1824 \pm 48$	$8420 \pm 260$
	FON-070	$70 \pm 2$	$1168 \pm 33$	$5500 \pm 170$
	FON-115	$115 \pm 2$	$874 \pm 25$	$4210 \pm 140$
	FON-190	$190 \pm 2$	$557 \pm 17$	$2122 \pm 78$
	FON-300	$300 \pm 2$	$523 \pm 16$	$1717 \pm 59$

	FON-500	500 ± 2	338 ± 11	1187 ± 65
T11	SOL-028	28 ± 2	1044 ± 29	5580 ± 170
41.4908, -5.6197	SOL-055	55 ± 2	671 ± 21	3540 ± 120
656 m a.s.l.	SOL-070	70 ± 2	580 ± 19	3340 ± 110
	SOL-100	100 ± 2	612 ± 22	3210 ± 110
	SOL-150	150 ± 2	458 ± 15	2090 ± 68
	SOL-300	300 ± 2	451 ± 15	2081 ± 76
	SOL-500	500 ± 2	368 ± 12	1357 ± 46
T12	ISI-020	20 ± 1	939 ± 29	4070 ± 130
41.4735, -5.3685	ISI-040	40 ± 1	787 ± 26	3920 ± 120
657 m a.s.l.	ISI-070	70 ± 2	642 ± 21	2855 ± 100
	ISI-110	110 ± 4	446 ± 14	1955 ± 69
	ISI-190	190 ± 4	376 ± 12	1314 ± 62
	ISI-300	300 ± 5	242.3 ± 8	736 ± 59
	ISI-02-500	500 ± 5	261.6 ± 9	829 ± 45

---

332

### 333 3.3.CSEB age model

334 The  $^{10}\text{Be}$  and  $^{26}\text{Al}$  concentrations measured in the profiles allowed us to model the  
335 shape of the theoretical in-situ produced cosmogenic nuclide signature with sample  
336 depth since terraces were deposited, and the construction of a chronological framework  
337 compatible with the cosmogenic nuclide signature measured. A Monte Carlo simulation  
338 of random models distributed in a window of 0–10 Ma was run in MATLAB<sup>®</sup> to find  
339 the chi-square values of the models that best fit the concentrations measured in our  
340 profiles. Monte Carlo simulations were run until 300 models fitting the 1-sigma  
341 confidence interval were found. Chi-squared minimization was performed for the  
342 models fitting the 1-sigma confidence interval (Rodés et al., 2014). The *in situ*  
343 production rate of cosmogenic  $^{10}\text{Be}$  and  $^{26}\text{Al}$  at each sampling site was determined  
344 considering the constant production rate model of Stone (2000) and apparent attenuation  
345 length values calculated from muonic production rate cross-sections generated using the  
346 code from the online calculator formerly known as the CRONUS-Earth online  
347 calculator v 2.3 (Balco et al., 2008; Table II). Uncertainties related to cosmogenic  
348 nuclides half-life and production rate were not included in age calculations, involving  
349 that uncertainties reported for burial durations shall be considered as internal  
350 uncertainties. The transmission of half-life and production rate uncertainties would  
351 impact the exposure ages by 10% or less, which is negligible compared to uncertainties  
352 of the obtained exposure ages.

353 A first modeling was performed without imposing geological constraints relative to  
354 the preservation degree of the surface. However, as the terrace preservation is a key

355 factor in determining individual terraces ages (onset of terrace surface exposure),  
 356 further models were run limiting the maximum lowering of each surface to better  
 357 constraint the exposure age of terrace surfaces. Maximum lowering values assumed in  
 358 the final CSEB age model are discussed in the results section with regards of soil  
 359 evidence and lowering measurements.

360 Table II.-  $^{10}\text{Be}$  -  $^{26}\text{Al}$  local production rates (P) and attenuation lengths (A) for spallation (sp), slow  
 361 muons (sm) and fast muons (fm) according to Stone (2000) and using the code from CRONUS Calc v 2.3  
 362 (<https://hess.ess.washington.edu>; Balco et al., 2008). Catchment production rates were estimated using the  
 363 average elevation of the source (1300 m) and the same latitude as the sampling sites because the Duero  
 364 Basin is E-W trending.

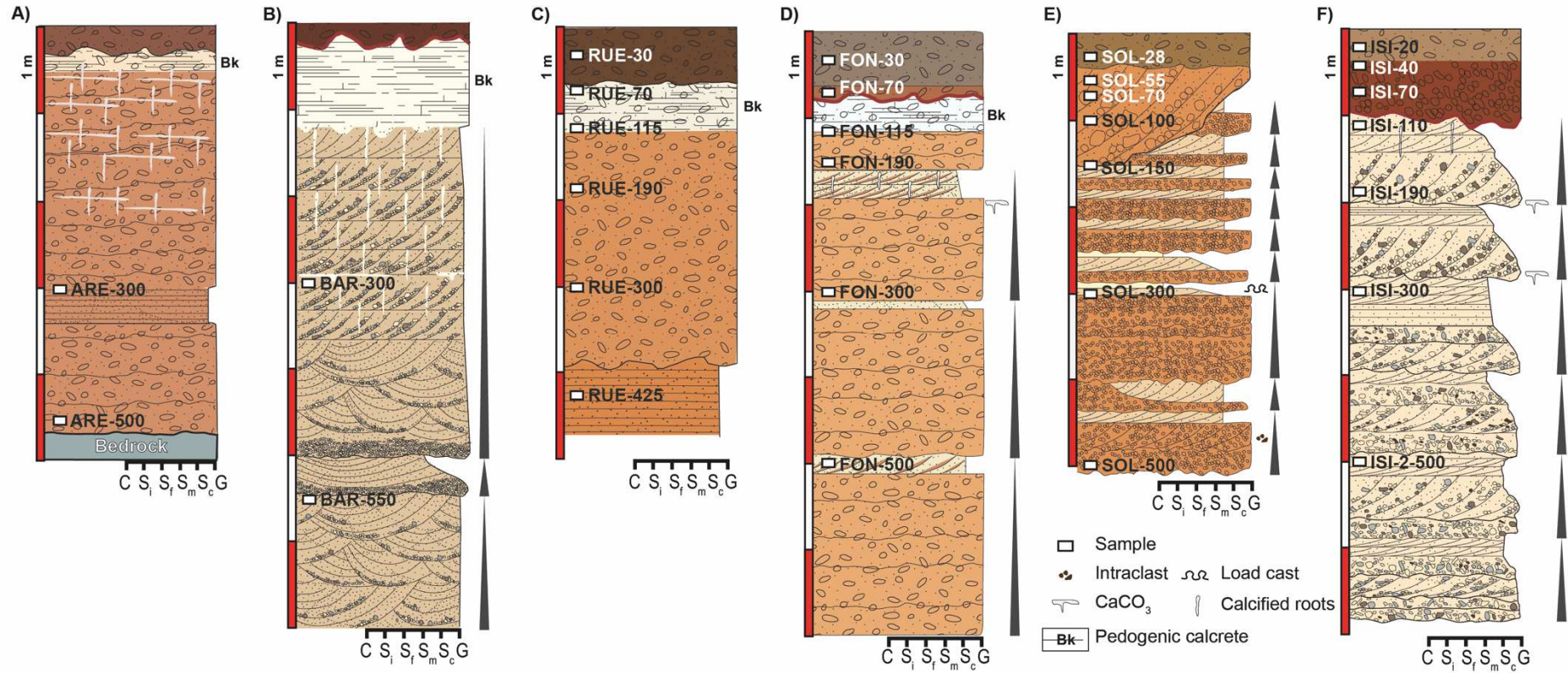
Location	Isotope	Psp ( $\text{at}\cdot\text{g}^{-1}\cdot\text{a}^{-1}$ )	Psm ( $\text{at}\cdot\text{g}^{-1}\cdot\text{a}^{-1}$ )	Pfm ( $\text{at}\cdot\text{g}^{-1}\cdot\text{a}^{-1}$ )	Asp ( $\text{g}\cdot\text{cm}^{-2}$ )	Asm ( $\text{g}\cdot\text{cm}^{-2}$ )	Afm ( $\text{g}\cdot\text{cm}^{-2}$ )
Basin source	$^{10}\text{Be}$	11.1655	0.0663	0.0491	160	859.1591	1606.500
	$^{26}\text{Al}$	75.3295	0.7522	0.3381	160	859.1591	1606.500
ARE	$^{10}\text{Be}$	7.5358	0.0538	0.0441	160	1002.8100	1775.0137
	$^{26}\text{Al}$	50.8407	0.6105	0.3042	160	1002.8100	1775.0137
BAR	$^{10}\text{Be}$	7.4098	0.0534	0.0439	160	1021.5003	1819.2790
	$^{26}\text{Al}$	49.9910	0.6050	0.3029	160	1021.5003	1819.2790
RUE	$^{10}\text{Be}$	7.2586	0.5028	0.0437	160	1016.4472	1784.2750
	$^{26}\text{Al}$	48.9709	0.5983	0.0433	160	1016.4472	1784.2750
FON	$^{10}\text{Be}$	6.9952	0.0517	0.0433	160	1041.6347	1830.8945
	$^{26}\text{Al}$	47.1941	0.5866	0.2982	160	1041.6347	1830.8945
SOL	$^{10}\text{Be}$	6.7157	0.0506	0.0428	160	1060.3815	1852.4256
	$^{26}\text{Al}$	45.3082	0.5740	0.2950	160	1060.3815	1852.4256
ISI	$^{10}\text{Be}$	6.7175	0.0506	0.0428	160	1060.1647	1852.1961
	$^{26}\text{Al}$	45.3200	0.5742	0.2950	160	1060.1647	1852.1961

## 365 4. Results

### 366 4.1. Sampled terrace depth profiles: sedimentology and soil characteristics

367 Terraces T2, T3, T6, and T10 were sampled along cross section 1, located ca. 70-80  
 368 km east from the WCB (Figures 4 and 5). Fluvial sediment thickness ranges between  
 369 4.2 and 4.7 m in terraces T2 and T6, and reaches up to 7 m in terrace levels T3 and T10  
 370 (Figure 4). Fluvial terraces T2 and T3 are lying directly on top of the Miocene bedrock,  
 371 which locally consists of grey clay and marls. Fluvial sequences sampled in terraces T2,  
 372 T6 and T10 are composed by reddish grain-supported cobble and gravel sediments with  
 373 sandy matrix, displaying massive strata or parallel to low-angle bedding, and locally  
 374 cobble imbrications. Some few centimeters-thick intercalations of sand with sparse  
 375 gravels are also present, showing parallel bedding (T2 and T6) or planar cross-bedding  
 376 (T10). These terraces probably represent the stacking of ancient river bars in a braided

377 fluvial system of high flow regime. Meanwhile, the sequence of terrace T3 is richer in  
378 sandy intervals compared to T2, T6 and T10. Particularly, T3 is composed by  
379 decametric to centimetric sets of sand and gravel sediments showing normal graded  
380 stratification, and displaying through cross-bedding close to the base and planar cross  
381 bedding towards the top. Thus, sediment architecture in T3 reflects a fluvial system of  
382 lower flow energy regime than in terraces T2, T6 and T10.



384

385

386

387

Figure 4.- Stratigraphic sections of the sampled terraces showing the distribution of samples in each terrace profile (grains size key is: C- clay; S<sub>i</sub>- silt; S<sub>f</sub>- fine sand; S<sub>m</sub>- medium sand; S<sub>c</sub>- coarse sand; G- gravel): A) T2 at Arentis quarry; B) T3 at Barbado Martín quarry; C) T6 at an old extraction area close to Rueda; D) T10 at Foncastin quarry; E) T11 at Sola e Hijos quarry; and F) T12 at Isidro quarry.



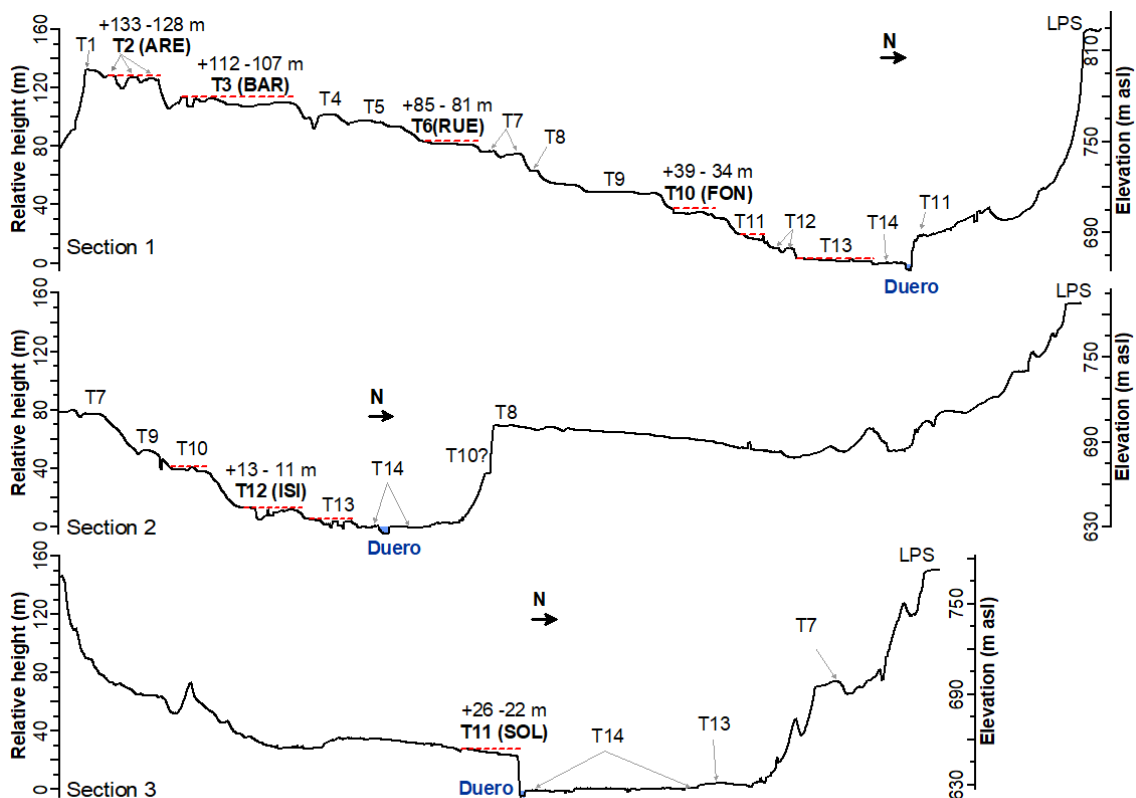
388 The youngest terraces (in terms of relative age) targeted for sediment depth profile  
389 sampling are T11 and T12, respectively sampled at cross sections 2 and 3 placed ca. 22  
390 and 42 km upstream from the Arribes knickzone (Figures 2 and 5). The sequence of  
391 T11 at SOL sampling site is 5.5 m-thick and includes alternations of reddish gravel  
392 units and yellowish sand and clay intervals arranged as normal graded sequences  
393 (Figure 4). The thickness of gravel units decreases from metric-decametric to  
394 centimetric beds upwards, mostly showing massive or parallel stratification and  
395 eventually displaying cross-bedding and muddy intraclasts. Gravel units alternate with  
396 thinner units of coarse-medium sand that gradually decrease in grain size towards the  
397 top to fine sand, silt and clay. Deformation structures such as load casts are visible in  
398 the clay intervals. Altogether, they are arranged as stacked normal graded sequences. A  
399 channel infill cross-cut the sequence previously described in the uppermost 1.5 m of the  
400 profile, composed by cross-bedded cobble and gravel sediments with sandy matrix. We  
401 interpret the lowest part of the sequence as the floodplain facies adjacent to the river  
402 channel infill. Finally, the youngest terrace level sampled, T12, is ca. 7 m in thickness.  
403 It is mostly composed by cross-bedded cobble, gravel and coarse sand sediments  
404 arranged as normal graded sequences. The uppermost part of the sequence culminates  
405 with coarse to medium sand beds displaying parallel or planar cross-bedding. The  
406 fluvial flow regime would be comparable or slightly more energetic than during the  
407 formation of T3 considering the grain size and sediment structures identified in the  
408 field.

409 Soils in the sampled terraces are generally around 1–1.15 m-thick (T3, T6, T10,  
410 T12) independently from their relative age, and exceptionally thinner than 1m in some  
411 terraces (0.5 m-thick in T2 and 0.4 m thick in T11; Figure 4) most likely due to post-  
412 soil formation erosion. Two similarities were noticed between the soils developed in the  
413 sampled terraces. First, the presence of an argillic horizon with intense dark red  
414 coloring, which is directly exposed to the surface in the oldest terraces T2 and T3, or at  
415 the base of a dark-brown argillic horizon (horizon B) in the intermediate (T6) and low  
416 terraces (T10 and T12). Second, the occurrence of a well-developed petrocalcic horizon  
417 (cemented by calcium carbonate) below the dark red argillic horizon in terraces T2 (20  
418 cm-thick), T3 (100 cm-thick), T6 (50 cm-thick), and T10 (40 cm-thick), starting at  
419 depths of 30-20 cm in the highest terraces (T2-T3) and at 70 cm in T6 and T10 (Figure  
420 4 A-D). It is worth mentioning that these two features are missing in the soil profile at  
421 the sampling site of T11, where the soil shows a brown argillic horizon B ca. 40 cm-

422 thick. Previous studies have classified the soils in the study area as Alfisols (Pérez-  
 423 González, 1982). More specifically they could correspond to Xeralfs, which are typical  
 424 of Mediterranean-type climate regimes and usually remain dry for extended periods in  
 425 summer (Soil Survey Staff, 2015).

426 *4.2. Terrace surface preservation and maximum lowering estimates*

427 Across Duero valley profiles passing through the sampling sites show the vertical  
 428 height of terrace scarps between successive levels (Figure 5). Although their top  
 429 surfaces are relatively well preserved in the study area, they show evidence of runoff  
 430 erosion and deflation (like blowout depressions up to 2 m deep and ventifacts),  
 431 indicating that erosion was locally important. Moreover, terraces might be prone to  
 432 burial by slope deposits and tributary fans from adjacent terrace levels (Mather et al.,  
 433 2017), but this is not an issue at our particular sampling sites. In order to constrain the  
 434 exposure age of terrace surfaces in the CSEB model, we limit the maximum lowering  
 435 experienced by each surface based on geological evidence.



436  
 437 Figure 5.- Sections of the Duero river crossing the sampling sites (see Figure 2 for the exact location of  
 438 each section). They show the full sequence of terrace levels preserved in each area and the spatial  
 439 relationships between them and with the modern floodplain (reference level to calculate the relative  
 440 height) and the LPS erosional surface to the North. Red dashed lines indicate the possible position of  
 441 original terrace top surfaces, providing a minimum estimate for the post-depositional maximum lowering  
 442 of the surface.

443 A first estimate of the true maximum lowering values of the sampled surfaces was  
444 done measuring the altitude difference between the terrace top surface at the sampling  
445 point and the maximum altitude observed in the surrounding areas of the same terrace  
446 outcrop. Assuming that the original terrace surface was flat (represented by red dashed  
447 lines in Figure 5), total lowering estimates up to ~5 m for T2 (ARE), ~3.5 m for T3  
448 (BAR), ~3 m for T6 (RUE) and T10 (FON), ~4 m for T11 (SOL), and ~1.5 m for T12  
449 (ISI) were inferred. Additional lowering linked to the erosion of the highest portion of a  
450 terrace top surface is difficult to infer due to the lack of indicators. However, since  
451 evidence of fill terraces was not found at the studied sites, denudation would be limited  
452 to the height difference between the highest sectors of a terrace top surface and the base  
453 of an immediately higher terrace. Therefore, no more than ~3 m of additional erosion  
454 would be possible in terrace T2 (ARE), ~15 m for terrace T3 (BAR), ~7 m for terrace  
455 T6 (RUE), ~8-6 for terrace T10 (FON), and ~5 m for terrace T12 (ISI). In the case of  
456 terrace T11 (SOL), the lack of higher terrace levels at Villalazán section makes  
457 impossible a direct measurement, but long profile analysis based on terrace levels  
458 preserved in the area shows an increasing trend in height difference between terrace  
459 levels T10 and T11 towards the WCB, placing the corresponding terrace scarp between  
460 ~15–10 m (Rodríguez-Rodríguez et al., 2020). Considering that the maximum thickness  
461 of fluvial sediments observed for terrace T10 is 7 m, a total lowering in the range ~8–3  
462 m can be inferred for T11 (SOL).

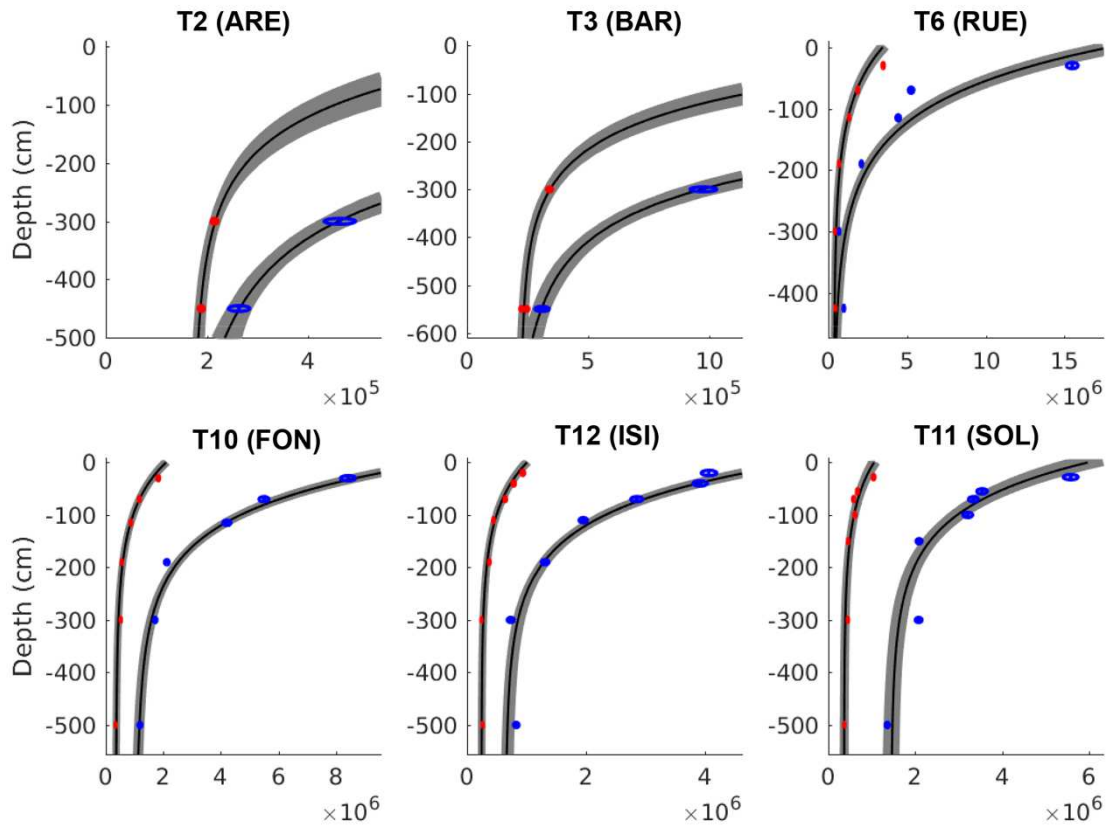
463 An alternative scenario of surface lowering was inferred from the soil characteristics  
464 observed in the different terraces (number and thickness of horizons preserved, presence  
465 of pedogenic carbonates). Terraces T2 to T10 contain pedogenic calcrete horizons (Bk),  
466 reaching ~0.2 m in thickness in T2 (ARE), ~1 m in T3 (BAR), and ~0.4-0.5 m in T6  
467 (RUE) and T10 (FON). Pedogenic calcrete formation might follow different paths  
468 depending on the local interplay between erosion, deposition and diagenesis (Alonso-  
469 Zarza, 2003), occasionally leading to the aerial exposure of the calcrete horizon if  
470 erosion overcomes local sedimentation (which is not observed in the studied terraces).  
471 As all are soils developed from similar parental materials and in an area of  
472 homogeneous climate conditions, assuming a zero-erosion scenario it would be  
473 expected that the thickness of the Bk horizon would decrease according to the relative  
474 age sequence because the oldest terraces have had more time to developed and have  
475 experienced the same climatic variations as those developed at lower levels in the

476 staircase. For instance, the Bk horizon in terrace T2 (ARE) should be at least 0.8 m  
477 thicker than it actually is to be similar to that preserved in terrace T3 (closest level  
478 placed right below T2). Regarding the location of the Bk horizon in the soils, the upper  
479 depth of the Bk horizon in the different terraces is found at ~0.3 m in T2 (ARE), ~0.2 m  
480 in T3 (BAR), and ~0.7 m in T6 (RUE) and T10 (FON). Taking as reference both the  
481 thickness and the depth of the upper Bk horizon's top in terraces T6 and T10, which  
482 show identical values, the oldest terraces T2 and T3 would have experienced a total  
483 surface lowering of 1.2 m and 0.5 m respectively. The lowest terraces T11 (SOL) and  
484 T12 (ISI) lack a Bk horizon and, hence, the single criteria available are the number and  
485 thickness of horizons preserved in the youngest terrace T12. The soil in terrace T12  
486 (ISI) is ~40 cm thicker and better developed (up to three well distinguished horizons)  
487 than the soil developed in terrace T11 (SOL) providing a minimum lowering estimate  
488 for the latest. Finally, for terraces T6, T10 and T12, a total surface lowering value of 0.2  
489 m has been arbitrarily assumed to avoid an unrealistic null value. The soil-based  
490 scenario simplifies factors involved in soil formation (especially at local level, which  
491 hampers a soil-based lowering estimation with confidence), but it offers an alternative  
492 scenario where total surface lowering since terrace abandonment is minimal instead of  
493 zero. The two lowering scenarios showcase well how this parameter affects exposure  
494 age interpretation.

#### 495 4.3. Age model results

496 The  $^{10}\text{Be}$ - $^{26}\text{Al}$  concentrations measured in six depth profiles were used to obtain  
497 multiple CSEB models for the Duero river terraces (Figure 6) considering different  
498 maximum lowering scenarios (Table III). Exposure ages for terraces T3 to T12 would  
499 range between 2.5 and 0.14 Ma when no constraint on maximum lowering is applied  
500 (only the morpho-stratigraphic order of the terraces was considered; Figure 7). If the  
501 maximum lowering is constrained based on geomorphological interpretations and  
502 measurements made in topographic sections, resultant exposure ages for the  
503 investigated terraces would be: 2265 to 265 ka for T3; 2210 to 478 ka for T6; 1078 to  
504 554 ka for T10; 549 to 117 ka for T11; and 217 to 150 ka for T12. However, exposures  
505 ages would be considerably younger when total surface lowering is estimated based on  
506 soil characteristics. Assuming a scenario of minimum total surface lowering (up to 0.2  
507 m) for terraces showing well-preserved soils and additional lowering increases for other  
508 terraces based on soil observations previously discussed, we obtained: 997 to 284 ka for  
509 T3; 611 to 449 ka for T6; 325 to 248 ka for T10; 171 to 100 ka for T11; and 142 to

510 115 ka for T12. The lack of degrees of freedom in the  $^{10}\text{Be}$ - $^{26}\text{Al}$  model of terrace T2  
 511 prevents the calculation of the surface exposure age uncertainty, and hence, results  
 512 displayed in Table III for the two lowering scenarios proposed would only constitute a  
 513 minimum estimate.



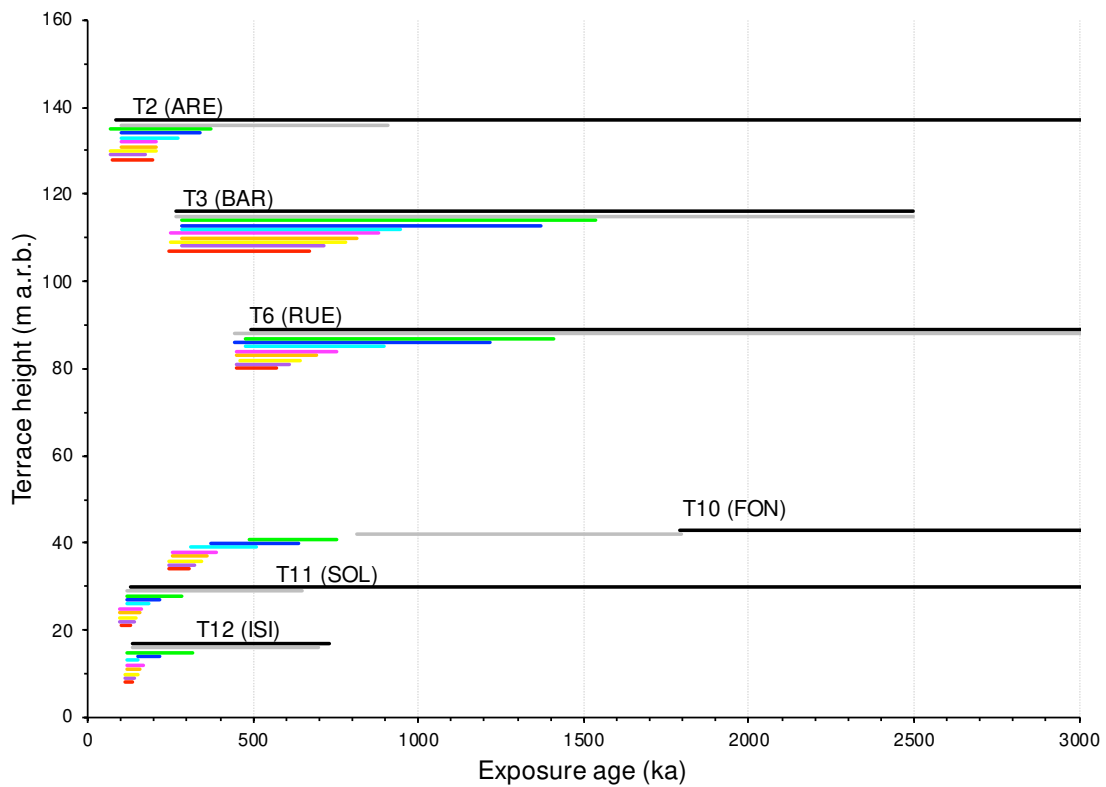
514

515 Figure 6.- Best fitting CSEB models (black lines) fitting the  $^{10}\text{Be}$  and  $^{26}\text{Al}$  concentrations (red and  
 516 blue ellipses) and CSEB models fitting the data within one-sigma confidence level (grey lines).



517 Table III.- CSEB dating age models of fluvial terraces sampled upstream from the WCB (sampling  
 518 locations are shown in Figure 2) considering three different scenarios of maximum lowering: free  
 519 (lowering limited to 100 m); maximum total lowering estimated from surface preservation; and maximum  
 520 lowering estimated from soil characteristics. Due to the lack of degrees of freedom in profile adjustment,  
 521 the exposure ages provided for T2 must be considered only minimum estimates.

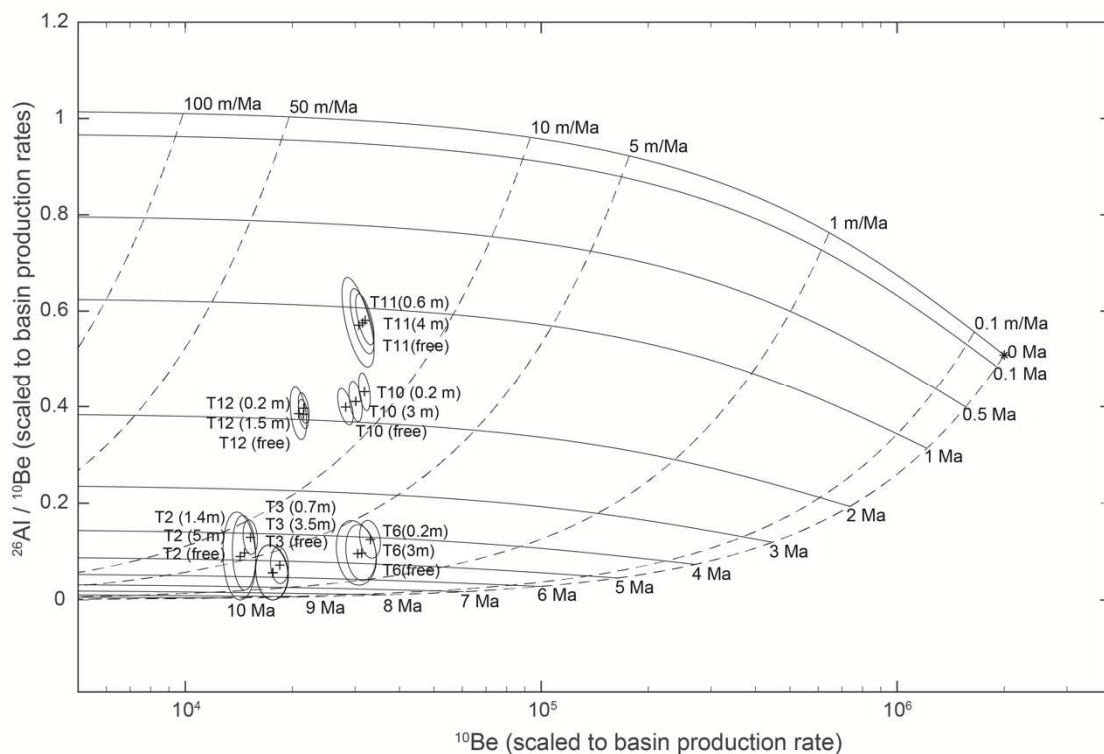
Terrace (lowering)	Relative height (m)	<sup>10</sup> Be inherited (10 <sup>4</sup> at.g <sup>-1</sup> )	<sup>26</sup> Al inherited (10 <sup>4</sup> at.g <sup>-1</sup> )	Basin denudation rate (m.Ma <sup>-1</sup> )	Exposure age (Ma)	Burial duration (Ma)	In situ denudation rate (m/Ma)
T2 (free)	+133-128	14.4-17.8	0-19.6	0-6.3	0.08-∞	3.67-10.10	<16.8
T3 (free)	+112-107	17.8-21.9	0-15.1	0-3.4	0.27-2.50	4.50-9.66	<4.4
T6 (free)	+85-81	30.0-38.9	7.2-37.5	0-3.1	0.50-∞	3.55-7.88	<1.6
T10 (free)	+39-34	30.3-33.5	79.3-93.1	8.0-10.7	1.79-∞	1.67-1.97	2.7-3.3
T11 (free)	+26-22	31.2-38.4	117.7-151.3	9.7-14.1	0.13-∞	0.94-1.39	0.5-8.7
T12 (free)	+13-11	22.3-24.8	53.4-69.5	10.4-12.7	0.14-0.73	1.72-2.15	<6.9
T2 (5 m)	+133-128	15.3-17.8	2.3-19.5	0.8-6.3	0.10-0.91	3.67-7.41	<15.1
T3 (3.5 m)	+112-107	17.8-22.0	0-15.2	0-3.4	0.27-2.27	4.48-9.67	<3.9
T6 (3 m)	+85-81	31.9-38.8	9.6-36.8	0.6-2.6	0.48-2.21	3.80-6.09	<1.6
T10 (3 m)	+39-34	32.6-35.5	85.8-103.6	7.6-9.5	0.55-1.08	1.65-1.94	2.7-3.3
T11 (4 m)	+26-22	32.9-38.4	126.7-151.2	9.7-13.4	0.12-0.55	0.92-1.34	<8.4
T12 (1.5 m)	+13-11	23.5-25.1	58.7-67.7	10.4-12.9	0.15-0.22	1.73-2.10	0.6-5.6
T2 (1.4 m)	+133-128	16.4-18.0	11.0-19.2	3.7-6.2	0.10-0.38	3.70-4.70	<9.9
T3 (0.7 m)	+112-107	19.6-22.0	4.8-15.5	1-3.3	0.28-0.98	4.47-6.53	<1.8
T6 (0.2 m)	+85-81	34.9-39.9	22.0-41.3	1.3-3.1	0.45-0.61	3.53-4.80	<0.4
T10 (0.2 m)	+39-34	34.7-37.4	96.3-114.1	7.7-9.4	0.25-0.33	1.54-1.83	<0.7
T11 (0.6 m)	+26-22	34.1-38.4	132.8-152.4	9.7-13.2	0.10-0.17	0.91-1.31	<4.2
T12 (0.2 m)	+13-11	23.5-25.2	60.7-70.1	10.5-12.6	0.12-0.14	1.74-2.03	<1.6



522  
 523 Figure 7.- Exposure ages of CSEB models fitting the data with no restrictions (black) and with limited  
 524 maximum total lowering of the terrace surfaces by 5 m (grey), 2 m (green), 1.5 m (blue), 1 m (cyan), 0.5

525 m (magenta), 0.4 m (orange), 0.3 m (yellow), 0.2 m (violet), and 0.1 m (red). Without lowering limitation  
 526 based on local evidence, the exposure age of most terraces (T3 to T12) is limited to 2.5 Ma based on the  
 527 maximum exposure age of T3 (ARE).

528 Burial durations reported for the studied terraces cover the time interval 0.9 to 2.0  
 529 Ma for terraces T10 (FON), T11(SOL) and T12 (ISI), while those found in the highest  
 530 terraces T6 (RUE), T3 (BAR) and T2 (ARE) cover a longer time interval of 3.5 to 9.6  
 531 Ma, evidencing longer transport times and complex exposure histories for the highest  
 532 terraces (Figure 8). Modelled basin denudation rates coetaneous to the oldest terrace  
 533 levels were much lower (up to 3–6 m·Ma<sup>-1</sup>) than those found (7.7–13.4 m·Ma<sup>-1</sup>) in the  
 534 youngest terraces.



535  
 536 Figure 8.- Inherited concentrations from table III plotted over a “banana plot” generated using the  
 537 average basin production rates, following Lal & Arnold (1985). The mountain ranges that limit the  
 538 Cenozoic Duero Basin worked as source area of sediments, located at a mean elevation of 1300 m  
 539 (estimation based on a 25 m resolution DEM from the Spanish National Institute of Geography).  
 540 Therefore, all <sup>10</sup>Be and <sup>26</sup>Al concentrations in this figure are scaled to surface production rates of 11.3 and  
 541 76.5 at·g<sup>-1</sup>·a<sup>-1</sup> respectively. This model allows us to classify the origin of these sediments in two groups:  
 542 an old group of sediments found in T2, T3 and T6 generated c. 5 Ma ago at a stable landscape (apparent  
 543 denudation rate < 10 m·Ma<sup>-1</sup>); and a young group of sediments found at T10, T11 and T12 generated 2–1  
 544 Ma ago at an active landscape (apparent denudation rate > 10 m·Ma<sup>-1</sup>).

## 545 5. Discussion

### 546 5.1. Pattern of erosion at basin scale and timing of basin opening

547 Calculated exposure time using the CSEB model of Rodés et al. (2014) combined  
 548 with the terrace staircase configuration (which indicates the relative age sequence)  
 549 provides a time reference for the starting point of incision and terrace formation as a

550 landform within the landscape (abandonment age). The abandonment age is limited to  
551 ca. 2.27–0.55 Ma in terrace T3 (+112–107 m), ca. 2.21–0.55 Ma in terrace T6 (+85–81  
552 m), ca. 1.08–0.55 Ma in terrace T10 (+39–34 m), 0.55–0.15 Ma in terrace T11 (+26–22  
553 m), and 0.22–0.15 Ma in terrace T12 (+13–11 m) for a lowering scenario constrained  
554 based on terrace topography and considering the relative age sequence (helps in  
555 narrowing the mathematical solutions of the CSEB model incompatible with the  
556 staircase configuration). Thus, terraces T3 to T6 would be ascribable to the Early  
557 Pleistocene, T10 to the Early-Middle Pleistocene and terraces T11 and T12 to the  
558 Middle Pleistocene. In contrast, the abandonment age is limited to ca. 0.98–0.45 Ma in  
559 terrace T3 (+112–107 m), ca. 0.61–0.45 Ma in terrace T6 (+85–81 m), ca. 0.33–0.25 Ma  
560 in terrace T10 (+39–34 m), 0.17–0.12 Ma in terrace T11 (+26–22 m), and 0.14–0.12 Ma  
561 in terrace T12 (+13–11 m) for a lowering scenario constrained based on soil  
562 characteristics, ascribing terraces T3 to T6 to the Early-Middle Pleistocene, terrace T10  
563 to the Middle Pleistocene, and terraces T11 and T12 to the Middle-Upper Pleistocene.  
564 Both scenarios provide an estimate for the timing of floodplain abandonment and  
565 terrace formation due to river incision that seem to be in agreement with previous  
566 interpretations, based on other techniques (OSL/TL, AAR, ESR and palaeomagnetic  
567 chronologies), which ascribed the full terrace staircase to the Pleistocene (Silva et al.,  
568 2017). They are also consistent with previous interpretations based on erosional  
569 surfaces developed on top of the Neogene infill sediments at the CDB. Close to the  
570 Iberian Chain, the top surface of the UPL shows karstification evidence that has been  
571 ascribed to the Late Miocene-Early Pliocene, due to a sedimentation break before the  
572 onset of the Neogene basin emptying (Benito-Calvo and Pérez-González, 2007). A  
573 second erosional surface (LPS) was formed at a lower elevation, on top of the LPL  
574 (Figure 2), which connects with the top surface of alluvial fans close to the source area  
575 of sediments in the Iberian Chain (Benito-Calvo and Pérez-González 2007). According  
576 to these authors, the LPS was formed prior to Pleistocene fluvial incision and could be  
577 considered Pliocene or Plio-Pleistocene. Thereafter, the highest terraces linked to the  
578 Duero river (T1, T2 and T3) were formed upstream from the Duero knickzone in the  
579 Early Pleistocene, starting at T1, the uppermost terrace preserved (+135–131 m respect  
580 the modern floodplain), which locates several tens of meters below the LPS (Figure 2).  
581 If the soil-based lowering scenario is considered, the ages obtained for the lowest  
582 terraces in our study area (hanging at +39 and +13 m) yield comparable depositional  
583 ages to those obtained through OSL by Cunha et al. (2019) in the DLR, which are

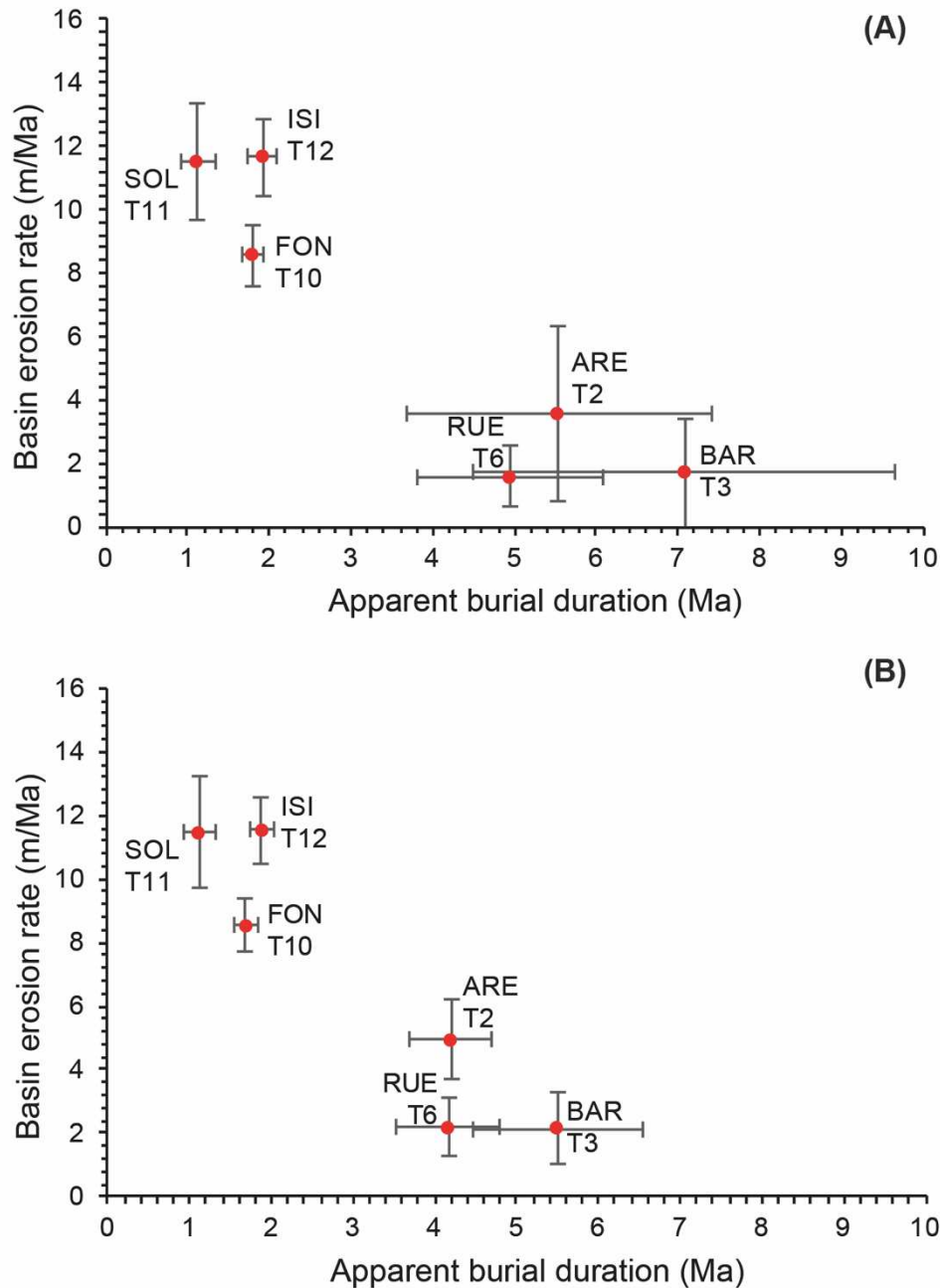
584 hanging between +53 and +13 m above the river bed between Pocinho and Barca  
585 d'Alva (ca. 360–12 ka). In contrast, the lowest terraces at the DLR are remarkably  
586 younger than the lowest terraces in the CDB when the lowering scenario based on  
587 terrace surface topography is considered. In any case, the DLR terraces are located  
588 downstream the Arribes knickzone at 200 m a.s.l. (500 m below the terrace staircase  
589 studied here), and point to several stages of terrace formation in a different stretch of the  
590 Duero long profile placed between the Duero lower and upper reaches (DLR and CDB  
591 respectively; Figure 1).

592 The inherited cosmogenic nuclides in a depth profile represent the signature of the  
593 sediment at the time of its deposition. In a simple burial history, sediments are eroded  
594 from the source area and deposited in a river terrace carrying an inherited cosmogenic  
595 signature that is proportional to the average exhumation rate at the source area and the  
596 travel time until being buried. However, more complex histories with multiple  
597 exhumation/burial episodes before the final burial event are also possible. Presumably,  
598 sediments found in the Duero terrace depth profiles come from a diverse source area  
599 located at the basin periphery, the highlands of the Cantabrian Mountains to the North,  
600 the Iberian Chain to the East and the Sistema Central to the South. Moreover, sediments  
601 eroded from the source area might have been mixed with recycled sediments from the  
602 Duero Cenozoic Basin, resulting in a material with mixed signature. Thus, inheritance-  
603 derived ages and basin erosion rates might inform on the evolution of the basin's  
604 bedrock denudation through time, while apparent burial durations may provide an  
605 estimate for the maximum travel time of sediments from the source area to the terrace in  
606 which they were found. These are key factors potentially related to the landscape  
607 response to exorheism.

608 Apparent burial durations calculated from the inherited  $^{10}\text{Be}$  and  $^{26}\text{Al}$   
609 concentrations in the highest terraces (T2, T3 and T6) indicate maximum sediment  
610 travel times in the range 3.5 to 9.7 Ma, while those found in the lowest terraces (T10,  
611 T11 and T12) yield values between 0.9 and 2.2 Ma (Figure 9). The several million-years  
612 difference between the maxima and minima values reported for the highest terraces is  
613 compatible with higher proportions of recycled sediments with inherited  $^{10}\text{Be}$ – $^{26}\text{Al}$   
614 concentrations. Also, apparent burial durations in the older terraces seem to be in  
615 reverse stratigraphic order, suggesting that the river was eroding a basin filled with  
616 sediments from top (younger sediments) to bottom (older sediments) when sediments  
617 included in T2 and T3 were formed (>3.5 Ma). Average denudation in the basin source

618 remained relatively low ( $<3\text{--}6\text{ m}\cdot\text{Ma}^{-1}$ ), suggesting that these palaeo-sediments were  
619 generated in a stable and relatively inactive basin.

620 Sediments included in the lowest terraces (T10, T11 and T12) indicate that average  
621 denudation rates at basin scale were already doubled ( $7.7\text{--}13.4\text{ m}\cdot\text{Ma}^{-1}$ )  $\sim 2\text{--}1\text{ Ma}$  ago.  
622 The lower proportion of inherited sediments and the acceleration of denudation rates at  
623 basin scale are both reflecting that sediments included in the lowest terraces contain a  
624 higher proportion of fresh sediments eroded from bedrock than those found in the  
625 highest terraces (Figure 9). A moderate mixed origin of sediments is then assumed for  
626 the lowest terraces possibly generated as the upper Duero River started to cut through  
627 bedrock materials under much more erosive conditions, with basin average denudation  
628 rates comparable to those found in other exorheic basins across Europe (e.g. Schaller et  
629 al., 2016a).



630

631 Figure 9.- Apparent basin denudation rates in the catchment area (y-axis) and apparent burial durations  
 632 (x-axis) are both calculated from inherited  $^{10}\text{Be}$  –  $^{26}\text{Al}$  concentrations measured in the terrace depth  
 633 profiles. They are both representative for the Duero Basin evolution and the exposure history of sediment  
 634 particles until being deposited in the studied terraces: (A) maximum lowering constrained based on  
 635 terrace surface topography and (B) maximum lowering constrained based on soil characteristics. In both  
 636 lowering scenarios, the highest terraces indicate lower basin denudation rates and older apparent burial  
 637 durations than in the lowest terraces, reflecting a considerable acceleration of incision along the upper  
 638 Duero river around 2 Ma, already in response to the basin opening to the Atlantic Ocean.

639 The opening of a closed basin involves a change in the long profile of the drainage  
 640 network as the incision wave migrates upstream from the opening point. The  
 641 acceleration of the basin denudation rates around ca. 4–2 Ma, and the marked



642 differences in the inherited signatures of the terrace deposits, evidence a timing delay  
643 between the basin opening and the arrival of the retrogressive erosive wave, nucleated  
644 at the opening zone, to the source area of sediments. This delay supports the hypothesis  
645 of the two trains of knickpoint waves traveling at different speeds through the soft  
646 Neogene sediment cover and the hard-Paleozoic bedrock (Struth et al., 2019). Hence,  
647 the low-propagating knickpoint wave travelling through the more resistant Paleozoic  
648 bedrock in the WCB basin likely regulates how fast the incision wave is transmitted  
649 upstream, while the terrace staircase formation across the basin will mostly respond to  
650 the fast-propagating waves that travel through the soft Neogene sediment cover.

651       Regarding the timing of the basin opening, compared to other Cenozoic basins from  
652 the Iberian Peninsula, the endo-exhoreic transition of the Duero Basin is likely to have  
653 occurred after that of the Ebro Basin (Antón et al., 2019). In the Ebro Basin, the fluvial  
654 network attained an advanced phase of adjustment since the opening of the foreland  
655 basin towards the Mediterranean Sea (Soria-Jáuregui et al., 2019). Resultant fluvial  
656 incision was able to induce as much as 630 m of uplift due to isostatic rebound, which is  
657 consistent with an opening age of 12.0–7.5 Ma obtained restoring the flexural isostatic  
658 compensation linked to infill erosion (García-Castellanos and Cruz-Larrasoña, 2015).  
659 In contrast, the Duero Neogene infill is poorly dissected and it pretty much preserves  
660 the pre-opening topography, with an estimated average surface lowering limited to  $65 \pm$   
661  $13$  m (Antón et al., 2019). Besides, the Duero river profile remains in disequilibrium  
662 illustrating a transient erosive response to the opening (Antón et al., 2014). The  
663 comparative analysis of chi-indices and knickpoint distribution for both basins  
664 highlights these differences, and the recalculated chi values once the drainage area is  
665 removed also supports the hypothesis of a recent endo-exorheic transition of the Duero  
666 Basin (Struth et al., 2019). Hence, a basin opening towards the Atlantic Ocean later than  
667 ca. 4-5 Ma, derived from our data, agrees with previous interpretations that assume a  
668 Plio-Pleistocene age for the basin switching from sedimentation to erosion due to its  
669 opening into the Atlantic Ocean (Benito-Calvo and Pérez-González, 2007; Silva et al.,  
670 2017; Antón et al., 2019; Cunha et al., 2019).

### 671 *5.2. Spatial variation of fluvial incision and denudation rates*

672       The CSEB model suggests that the erosive fingerprint of the basin endo-exorheic  
673 transition was important at the source area of sediments since at least 2–1 Ma ago,  
674 marked by the increase in apparent basin denudation rates and the increased proportion

675 of fresh sediments recorded in the lowest terraces. This interpretation is consistent with  
676 Electro Spin Resonance (ESR) chronologies reported for fluvial terraces in the Arlanzón  
677 and Arlanza valleys, two tributaries of the Duero river placed more than 130 km  
678 upstream from our study area (Table IV and Figure 10). In the Arlanzón River an ESR  
679 age of  $1.14 \pm 0.13$  Ma was reported for terrace T3 (+78–70 m), while the inferior levels  
680 provided the following results (Moreno et al., 2012): (i)  $0.78 \pm 0.12$  and  $0.93 \pm 0.10$  Ma  
681 for terrace T4 (+67–60 m); (ii)  $0.70 \pm 0.10$  Ma for terrace T5 (+54–50 m); (iii)  $0.40 \pm$   
682  $0.09$  Ma for terrace T8 (+35–26 m); and (iv)  $0.14 \pm 0.02$  Ma for terrace T11 (+13–12  
683 m). Similarly, the ESR chronology of the nearby Arlanza River yielded ages of  $0.79 \pm$   
684  $0.11$  Ma for terrace T5 (+79–73 m);  $0.70 \pm 0.07$  Ma for terrace T6 (+67–64 m);  $0.35 \pm$   
685  $0.04$  Ma for terrace T10 (+36–33 m); and  $0.23 \pm 0.03$  Ma for terrace T12 (+23–20 m),  
686 suggesting similar fluvial evolution in both tributaries (Moreno et al., 2016) (Table IV,  
687 Figure 10). In the Esla River, a tributary which converges with the Duero river ~50 km  
688 downstream from the study area, thirteen terrace levels were described with the highest  
689 terrace located at +160 m (Torrent, 1976). Upper terraces are associated to a Paleo-Esla,  
690 which switched its course to the west between ~0.52 Ma and 0.15 Ma (Schaller et al.,  
691 2016b). An age of ~1.04 Ma was assigned to the highest level by previous authors,  
692 while cosmogenic nuclides analysis in lower fluvial terraces yielded depositional ages  
693 of  $\sim 0.52 \pm 0.20$  Ma for the youngest Paleo-Esla terrace at +78–76 m and 0.16 to 0.08  
694 Ma for the lowest Esla terraces at +64–32 m to +8–7 m (Schaller et al., 2016b) (Table  
695 IV and Figure 10). Both datasets support the idea that in the tributary valleys close to  
696 the source area of sediments most terraces formed over the last ~1.5–1 Ma, while in our  
697 study area the studied terraces were most likely formed since 2.5–1 Ma (depending on  
698 the total surface lowering scenario assumed).

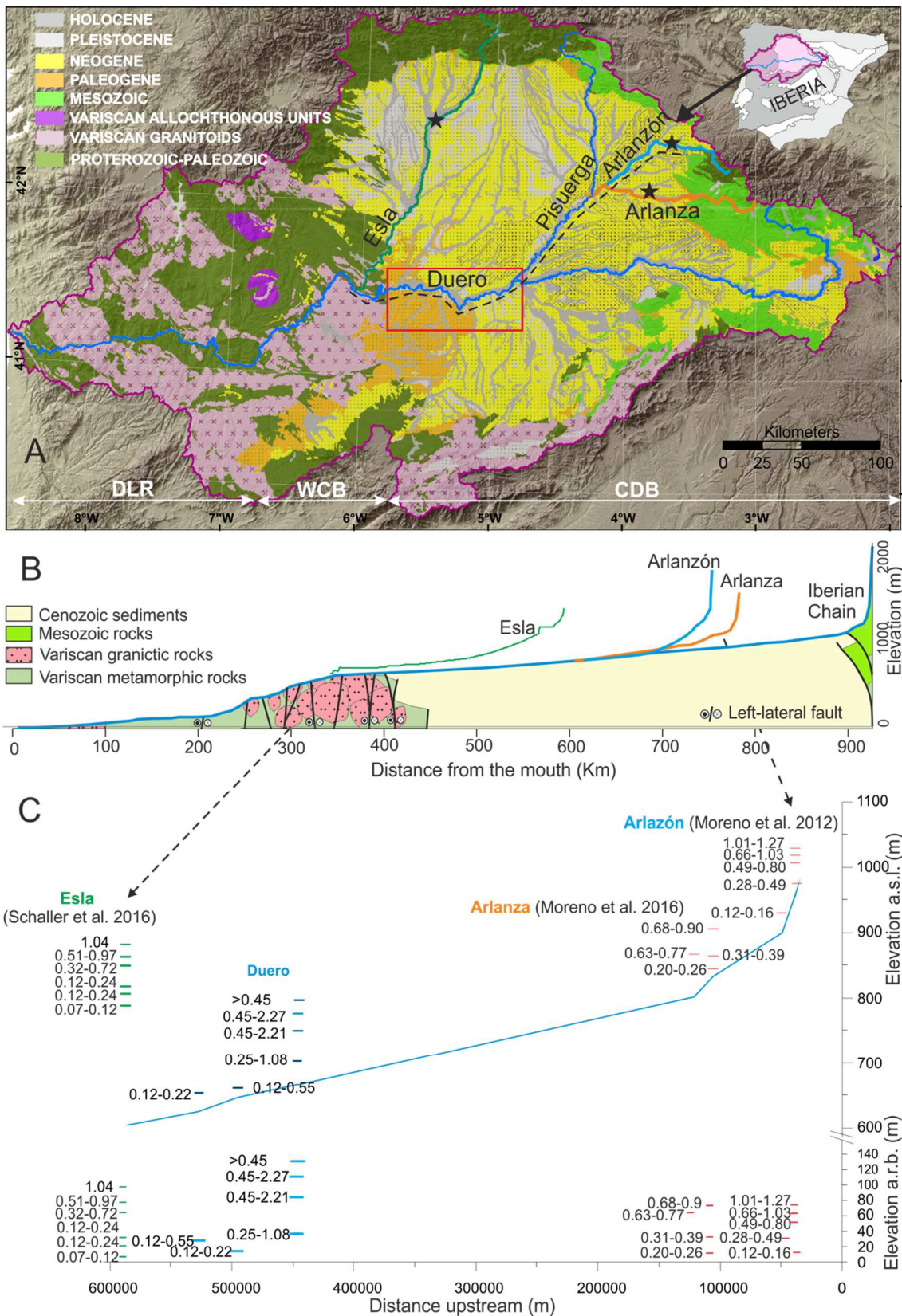
699  
700  
701  
702

Table IV.- Available chronological framework for the Duero fluvial network upstream the Arribes knickzone, including the Arlanzón, Arlanza and Esla tributaries. Incision rate estimations along the main channel for each of these rivers considering available terraces ages and maximum total incision observed for each terrace level at the specific sampling site. Terrace level names according to the references.

Valley	Terrace level	Terrace height (m)	Age (Ma)		Incision rate (m/Ma)		Reference
			min	max	max	min	
Arlanzón	T3	+78-70	1.01	1.27	77	61	Moreno et al. (2012)
		+67-60	0.66	0.9	102	74	
	T5	+67-60	0.83	1.03	81	65	
		+54-50	0.6	0.8	90	68	
		+54-50	0.63	0.77	86	70	
	T8	+54-50	0.49	0.67	110	81	
		+35-26	0.28	0.44	125	80	
		+35-26	0.31	0.49	113	71	
T11	+13-12	0.12	0.16	108	81	Moreno et al. (2016)	
Arlanza	T5	+79-73	0.68	0.9	116		88
	T6	+67-64	0.63	0.77	106		87
	T10	+36-33	0.31	0.39	116		92
Duero	T12	+23-20	0.2	0.26	115	88	This study
	T3 (3.5 m)*	+112-107	>0.55	2.27	<202	49	
	T6 (3 m)*	+85-81	>0.55	2.21	<153	38	
	T10 (3 m)*	+39-34	0.55	1.08	70	36	
	T11 (4 m)*	+26-22	>0.15	0.55	<173	47	
	T12 (1.5 m)*	+13-11	0.15	0.22	87	60	
	T3 (0.7 m)*	+112-107	>0.45	0.98	<249	115	
	T6 (0.2 m)*	+85-81	0.45	0.61	189	139	
	T10 (0.2 m)*	+39-34	0.25	0.33	157	120	
	T11 (0.6 m)*	+26-22	>0.12	0.17	<226	152	
Paleo-Esla	T12 (0.2 m)*	+13-11	0.12	0.14	113	92	Schaller et al. (2016b)
	G; f	+100-95	0.51	0.97	196	103	
	SK; h	+78-76	0.32	0.72	244	108	
+78-76		0.39	0.72	200	108		
Esla	P; j	+32	0.12	0.24	267	133	
	T20; l	+22-20	0.12	0.24	183	92	
	n	+8-7	0.07	0.12	114	67	

703

(\*) Maximum lowering scenario considered for each terrace surface in the exposure age calculation is provided in brackets.



704

705

706

707

708

709

Figure 10.- Synthesis of available chronological data on fluvial terraces for the Duero river and its tributaries: (A) location of dated terrace sequences in the context of the CDB (the rectangle marks the study area; stars indicate the location of other terrace sequences previously dated along the Esla, Arlanza and Arlanzón streams). (B) Long profile of the Duero river and the tributaries with chronological data on terrace sequences (Esla, Arlanza, Arlanzón). (C) Distribution and age (expressed in Ma) of terraces above

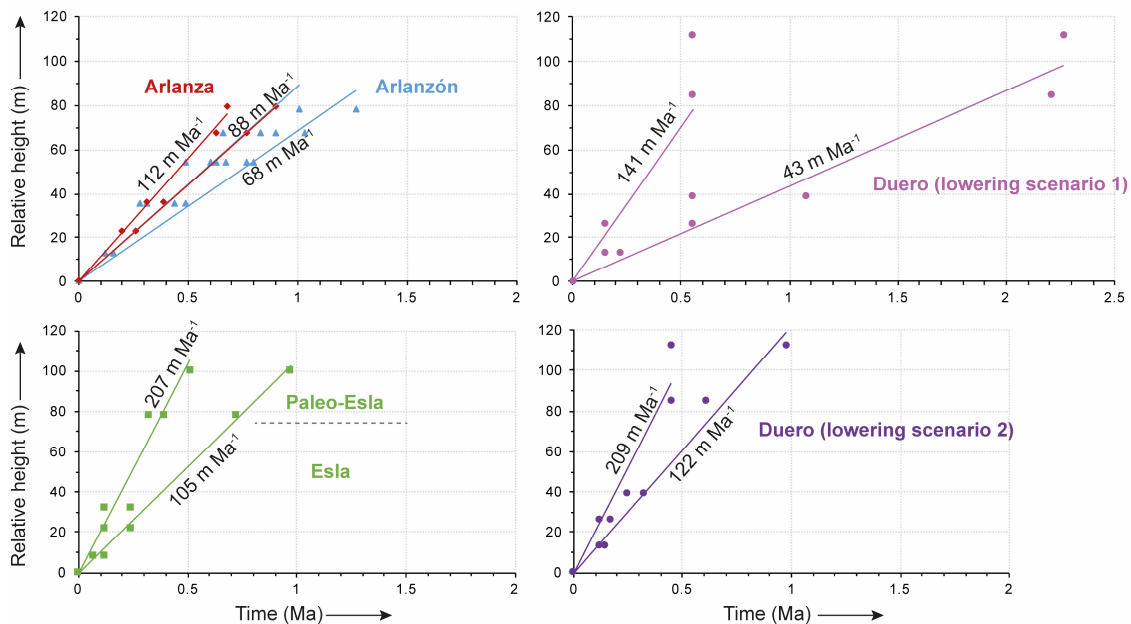
710 the river bed and at their position and elevation over the long profile integrating the Duero and the its  
711 tributaries upstream from the WCB up to the Arlanzón. Dashed line in A and arrows in B, show the  
712 stretch represented in the integrated long profiles. Chronological data on the Esla river are represented at  
713 its confluence's location with the Duero river.

714 River incision rates were estimated in the study area using the maximum relative  
715 height of dated terrace levels as a reference for total incision (up to +112 m) and terrace  
716 abandonment ages derived from the CSEB dating model (Table IV). Depending on the  
717 lowering scenario considered (Figure 11), time-averaged incision rates deduced from  
718 linear adjustment of dated terrace values would range between ca. 43–141 m·Ma<sup>-1</sup> since  
719 2.3 Ma (lowering scenario #1), or 122–209 m·Ma<sup>-1</sup> since 1 Ma (lowering scenario #2).  
720 These time-averaged incision values obtained close to the basin opening/overspill point  
721 seem in turn in agreement with the values obtained upstream. Close to the source area in  
722 the Iberian Chain, total incision along the Arlanzón and Arlanza tributaries attained up  
723 to 79–78 m over the last 1Ma, involving time-averaged incision rates in the order of 68–  
724 88 m·Ma<sup>-1</sup> and 88–112 m·Ma<sup>-1</sup>, respectively (Figure 11). In contrast, the Esla River  
725 attained a total incision up to 100 m for the same period of time as reported by Schaller  
726 et al. (2016a), involving time averaged incision rates in the range 105–207 m·Ma<sup>-1</sup> over  
727 the last 1 Ma, which are comparable or slightly lower than those obtained in our study  
728 area using the soil-based lowering scenario. These results support the diachronous  
729 character of terraces formed through knickpoint propagation as demonstrated in other  
730 studies (e.g. Stokes et al., 2002; Rixhon et al., 2011; Baynes et al., 2015; Finnegan,  
731 2013). However, the chronological data on time transgressive formation of terraces and  
732 basin denudation in the Duero catchment allow further interpretations to understand  
733 general-patterns and rates of landscape adjustment associated to basin scale endo-  
734 exorheic transitions.

735  
736  
737

Table V. - Summary of denudation rates and time-averaged incision rates in the Duero, Esla, Arlanza and Arlanzón sites (compiled in Table IV) considering different time periods. Lowering scenarios in the Duero River are based on terrace surface topography (1) and soils (2).

Time	Duero (scenario 1)	Duero (scenario 2)	Esla	Arlanza	Arlanzón
>3.5 Ma	Basin denudation rates <6 m/Ma (based on inherited $^{10}\text{Be}$ and $^{26}\text{Al}$ from terraces T2, T3 and T6)		Possibly low basin average denudation rates (based on high $^{10}\text{Be}$ inheritances between 0.14 and 0.3 M atoms/g from terraces in Schaller et al., 2016a)	Possibly slow basin denudation rates, as Arlanza and Arlanzón are inside the catchment of T2, T3, T6, T10, T11 and T12.	
Since 2-1Ma	Basin denudation rates rose between 8 and 13 m/Ma (based on inherited $^{10}\text{Be}$ and $^{26}\text{Al}$ from terraces T10, T11 and T12)	Incision rates between 36-49 to <202 m/Ma (based on maximum $^{10}\text{Be}$ and $^{26}\text{Al}$ deposition ages of T3, T6 and T10)			
Since 1-0.6Ma	Incision rates of 36-70 m/Ma (based on $^{10}\text{Be}$ and $^{26}\text{Al}$ deposition ages of T10)	Incision rates of 115- <249 m/Ma (based on $^{10}\text{Be}$ and $^{26}\text{Al}$ deposition ages of T3)	Incision rates of 103-196 m/Ma based on terrace $^{10}\text{Be}$ deposition ages of paleo-Esla terraces (Schaller et al., 2016b).	Incision rates c. 87-116 m/Ma based on ESR age of terraces T5 and T6 (Moreno et al., 2016)	Incision rates c. 61-102 m/Ma based on ESR ages of terraces T3, T4 and T5 (Moreno et al., 2012)
Since 0.6-0.2 Ma	Incision rates of <173 m/Ma (based on $^{10}\text{Be}$ and $^{26}\text{Al}$ deposition ages of T11)	Incision rates of 120-189 m/Ma (based on $^{10}\text{Be}$ and $^{26}\text{Al}$ deposition ages of T6 and T10)	Incision rates c.108-200 m/Ma (based on terrace $^{10}\text{Be}$ deposition ages in Schaller et al., 2016b). Basin denudation of 60-56 m/Ma (Schaller et al., 2016b)	Incision rates of 88-116 m/Ma based on ESR age of +64m terraces (Moreno et al., 2016)	Incision rates up to 125 m/Ma based on ESR ages of terraces T5, and T8 (Moreno et al., 2012)
Since <0.2 Ma	Incision rates of 60-87 m/Ma (based on $^{10}\text{Be}$ and $^{26}\text{Al}$ minimum deposition age of T12)	Incision rates of ca. 92 to <226 m/Ma (based on $^{10}\text{Be}$ and $^{26}\text{Al}$ minimum deposition age of T11 and T12)	Incision rates between 67 and 114 m/Ma based on $^{10}\text{Be}$ deposition age of terrace 12ESL007 (Schaller et al., 2016b). Basin denudation rates of 33-56 m/Ma (Schaller et al., 2016a)	—	Incision rate of 81-108 m/Ma based on ESR age of terrace T11 (Moreno et al., 2012)



738  
739  
740

Figure 11.- Comparison between terrace sequences preserved at specific sampling sites along the Arlanzón, Arlanza and Esla tributaries with that recorded along the main Duero river in our study area,



741 based on datasets compiled in Table V. For the Duero river, the two different lowering scenarios  
742 discussed in the main text are provided, which are based on terrace surface topography (1) and soil  
743 characteristics (2). Each pair of regression lines represent average incision rates at each site in the basin  
744 using the full dataset locally available.

745 Cyclic fluvial aggradation and entrenchment episodes are frequently interpreted as  
746 the response to sustained base-level lowering driven by a combination of tectonic and/or  
747 climatic fluctuations (e.g. Bridgland and Westaway, 2008; Cunha et al. 2008). The  
748 Duero Basin occupies a relatively stable tectonic setting where evidence of significant  
749 tectonic uplift since the late Miocene is absent (De Vicente and Vegas, 2009; Antón et  
750 al., 2010). Chronological data on fluvial terraces do not favor a straightforward  
751 interplay between climate and terrace formation. Nevertheless, the base level lowering  
752 associated at the basin opening seems the main mechanism linked to basin infill  
753 dissection and terrace staircase development. In a similar context, Bartz (2019) rule out  
754 climate as the main driver mechanism for fluvial aggradation in the Triffa basin (NE  
755 Morocco), suggesting that basin scale capture events might dominate a fluvial transient  
756 response. Previous works (e.g. Paola et al., 1992; Beaumont et al., 2000), indicate that  
757 each system has an intrinsic time response to recover the equilibrium after a climatic  
758 perturbation or a change in drainage connectivity. This time is scale-dependent but falls  
759 often in the order of millions of years (Whipple and Tucker, 1999; Pazzaglia, 2003,  
760 Whipple, 2001; García-Castellanos and Larrasoaña, 2015). Even for much smaller  
761 basins of 10 and 70 km<sup>2</sup> in Hatay Graben (Turkey) and the Apennines, Whittaker and  
762 Boulton (2012) estimate a fluvial response time in the order of 3–1 Ma. In the Duero  
763 river case, the configuration of the crystalline hard bedrock at the WCB might have  
764 contributed in delaying the time needed to recover a steady-state profile.

765 The recorded eastward progression of the incision wave generated in the opening  
766 area (Table VI), illustrates the erosional pattern expected in continental basins that  
767 underwent an endorheic to exorheic transition, (e.g. Antón et al., 2019; Bartz, 2019;  
768 Mather, 2000; Stokes et al., 2002, 2018; Soria-Jáuregui et al., 2019). A strong coupling  
769 between the rate of fluvial downcutting and orbital-forcing has been suggested for the  
770 Tagus and the Duero rivers, particularly since the establishment of the 100 ka  
771 eccentricity cycles (Silva et al., 2017). Our chronological results favor an increase of  
772 apparent basin denudation since ~2 Ma, but do not allow an accurate interpretation of  
773 the interplays between climate and terrace formation. We assume that changes in  
774 sediment supply related to climate cyclicity are superimposed onto the long-term base  
775 level lowering, which dominates the fluvial entrenchment in the area. The base level

776 drop resulting from the onset of exorheism generates knickpoint wave trains  
777 propagating upstream along the drainage system (Struth et al., 2019). In the Duero,  
778 immediately downstream of the study area, the incision is limited by the resistant  
779 lithology at the Arribes gorge (WCB, Figure 10), which regulates the transmission of  
780 successive knickpoint waves upstream. As the Duero attains incision at the basin outlet  
781 (WCB), the erosive wave propagates towards the basin center increasing the profile  
782 gradient. While the knickpoint progresses upstream, the fluvial system aggrades  
783 downstream to progressively balance the channel gradient. Successive incision waves,  
784 due to progressive incision at the basin outlet, will result in fluvial downcutting with the  
785 development of the inset Pleistocene river terrace sequence at the basin center and the  
786 propagation of the erosional signal along the tributary network to the catchment divide.  
787 This model is consistent with an enhanced erosion in the Esla catchment allowing  
788 higher incision rates and total incision (highest terrace at +100 m) than in the Arlanza-  
789 Arlanzón system placed further upstream (highest terrace ~80 m; Figures 10 and 11).  
790 Also, significant differences in terrace patterns and landscape dissection are observed in  
791 the main trunk (Rodríguez-Rodríguez et al., 2020), with the highest terraces only  
792 preserved upstream at the basin center (Figure 2). At a basin scale, the relatively low  
793 average denudation rates derived from the upper terraces are consistent with a null or  
794 scarce transmission of the erosive wave nucleated at the opening site along the  
795 catchment at that stage. In contrast, by the time of the lowest terraces formation (T10,  
796 T11 and T12) denudation rates doubled, suggesting the establishment of much more  
797 erosive conditions at basin scale and the arrival of the enhanced erosional signal to the  
798 basin source.

799 The Cenozoic Duero basin is an exceptional example to understand the evolution of  
800 sedimentary basins and longer-term landscape response associated to a continental scale  
801 drainage reorganization. Results provide a chronological framework for the terrace  
802 sequence and illustrate the main role of autogenic mechanisms in landscape dissection  
803 and terrace staircase formation in response to basin-scale endorheic to exorheic drainage  
804 transition.

## 805 **6. Conclusions**

806 Paired  $^{10}\text{Be}$ - $^{26}\text{Al}$  concentrations measured in six terrace depth profiles of the Duero  
807 fluvial terrace staircase upstream from the western margin of the Cenozoic basin

808 provide important insights about the timing of the endo-exorheic transition and  
809 subsequent basin evolution:

- 810 1) Inherited  $^{10}\text{Be}$ - $^{26}\text{Al}$  concentrations suggest an increase in basin denudation rates  
811 after the basin opening to the Atlantic Ocean. Basin average denudation rates  
812 remained relatively low ( $<3\text{--}6\text{ m}\cdot\text{Ma}^{-1}$ ) until at least 3.5 Ma, showing higher  
813 proportions of recycled sediments, and then experienced an acceleration at ca.  
814 2–1 Ma ( $8\text{--}13\text{ m}\cdot\text{Ma}^{-1}$ ).
- 815 2) Terrace surface exposure ages obtained with the CSEB model can be  
816 constrained by limiting the total amount of surface lowering based on  
817 geomorphic and soil indicators. Future studies based on alternative dating  
818 methods might help to better constrain the most probable post-depositional  
819 lowering scenario for the studied terraces. In any case, the CSEB model favors  
820 Pleistocene ages ( $<2.5\text{ Ma}$ ) for the terraces belonging to the Duero staircase.
- 821 3) The apparent change in basin-scale denudation rates is in agreement with the  
822 propagation of an eastward erosive wave through the study area as proposed by  
823 Struth et al. (2019), nucleated at the western fringe of the basin during the endo-  
824 exorheic transition. This wave might have arrived at the basin source between  
825  $\sim 1$  to 2 Ma ago, being T10 the oldest terrace clearly containing sediments that  
826 record the starting of the upper Duero incision in bedrock. This is consistent  
827 with previous chronologies reported for some of the oldest terraces preserved in  
828 tributary rivers like the Arlanzón, Arlanza and Esla, where the oldest terrace  
829 ages are around 1 Ma.
- 830 4) Time-averaged incision rates over the last million years display the highest  
831 values close to the opening site of the CDB ( $122$  to  $<250\text{ m}\cdot\text{Ma}^{-1}$  in the Duero  
832 River;  $105\text{--}207\text{ m}\cdot\text{Ma}^{-1}$  in the Esla River), and the lowest values close to the  
833 eastern boundary of the catchment ( $68\text{--}88\text{ m}\cdot\text{Ma}^{-1}$  in the Arlanzón River).

834 Altogether, these findings support the diachronous character of landscape  
835 dissection through knickpoint propagation from the opening zone and illustrate the time  
836 transgressive formation of terraces along the Duero catchment.

### 837 **Acknowledgements**

838 This is a MITE contribution (Spanish Government *Plan Estatal de Investigación*  
839 *Científica y Técnica y de Innovación*, CGL2014-59516 & PR2011-0044). At the time of  
840 paper writing, L. Rodríguez-Rodríguez was recipient of an outgoing post-doctoral grant

841 of the Clarín-Cofund program (Ref. ACA-17-19), financed jointly by the regional  
842 government of Principality of Asturias and the 7<sup>th</sup> WP of the European Union–Marie  
843 Curie Actions. The ASTER AMS national facility (CEREGE, Aix en Provence) is  
844 supported by the INSU/CNRS, the ANR through the "Projets thématiques d'excellence"  
845 program for the "Equipements d'excellence" ASTER-CEREGE action and IRD.  
846 Candela Pastor-Martín is thanked for the GIS technical support (funded under grant  
847 PEJ-2014-A-93258). We thank Martin Stokes and Zsófia Ruzsiczay-Rüdiger for their  
848 constructive reviews on the manuscript, which helped us to improve the initial version.  
849 We are also thankful to the enterprises Arentis Aridos S.L., Barbado Martín S.L.,  
850 Aridos Sola e Hijos S.L., and Jose Isidro Torres S.L. for allowing us to sample fluvial  
851 sediments in exposed terrace sections at their exploitation quarries.

## 852 **References**

- 853 Alonso, J.L., Pulgar, J.A., García-Ramos, J.C., Barba, P., 1996. Tertiary basins and  
854 Alpine tectonics in the Cantabrian Mountains (NW Spain). In: Friend, P.F., Dabrio,  
855 C.J. (Eds.), Tertiary Basins of Spain: the stratigraphic record of crustal kinematics.  
856 Cambridge University Press, Cambridge, pp. 214–227.
- 857 Alonso-Gavilán, G., Armenteros, I., Carballeira, J., Corrochano, A., Huerta, P.,  
858 Rodríguez, J., 2004. Cuenca del Duero. In: Vera, J.A. (Ed.), Geología de España.  
859 IGME, Madrid, pp- 550-556.
- 860 Alonso Gavilan, G., Dabrio, C.J., Mediavilla, R.M., Armenteros, I., 1989. Procesos  
861 sedimentarios y desarrollo de Sand Flats en ríos arenosos del Eoceno del suroeste de  
862 la depresion del Duero. *Studia Geologica Salmanticensia*, Extraordinario No. 5, 159-  
863 176.
- 864 Alonso-Zarza, A.M., 2003. Palaeoenvironmental significance of palustrine carbonates  
865 and calcretes in the geological record. *Earth-Science Reviews* 60, 261-298.
- 866 Alonso-Zarza, A.M., Armenteros, I., Braga, J.C., Munoz, A., Pujalte, V., Ramos, E.,  
867 Aguirre, J., Alonso Gavilan, G., Arenas, C., Baceta, J.I., Carballeira, J., Calvo, J.P.,  
868 Corrochano, A., Fornos, J.J., Gonzalez, A., Luzon, A., Martin, J.M., Pardo, G.,  
869 Payros, A., Perez, A., Pomar, L., Rodriguez, J.M., Villena, J., 2002. Tertiary. In: W.  
870 Gibbons, T. Moreno (Eds.), *The geology of Spain*. Geological Society, Bath, United  
871 Kingdom, pp. 293-334.
- 872 Antón, L., Muñoz-Martín, A., De Vicente, G., 2010. Alpine paleostress reconstructions  
873 and active faulting in Western Iberia. *Central European Journal of Geosciences* 2,  
874 152-164.

- 875 Antón, L., De Vicente, G., Muñoz-Martín, A., Stokes, M., 2014. Using river long  
876 profiles and geomorphic indices to evaluate the geomorphological signature of  
877 continental scale drainage capture, Duero basin (NW Iberia). *Geomorphology* 206,  
878 250-261.
- 879 Antón, L., Muñoz-Martín, A., De Vicente, G., 2019. Quantifying the erosional impact  
880 of a continental scale drainage capture in the Duero Basin (NW Iberia). *Quaternary*  
881 *Research*, 91(2), 457-471.
- 882 Antón, L., Rodés, A., De Vicente, G., Pallàs, R., Garcia-Castellanos, D., Stuart, F.M.,  
883 Braucher, R., Bourlès, D., 2012. Quantification of fluvial incision in the Duero Basin  
884 (NW Iberia) from longitudinal profile analysis and terrestrial cosmogenic nuclide  
885 concentrations. *Geomorphology*, 165–166, 50-61.
- 886 Arnold, M., Merchel, S., Bourlès, D., Braucher, R., Benedetti, L., Finkel, R.C.,  
887 Aumaître, G., Gott dang, A., Klein, M., 2010. The French accelerator mass  
888 spectrometry facility ASTER: Improved performance and developments. *Nuclear*  
889 *Instruments and Methods in Physics Research B*, 268, 1954-1959.
- 890 Balco, G., 2017. Production rate calculations for cosmic-ray-muon-produced  $^{10}\text{Be}$  and  
891  $^{26}\text{Al}$  benchmarked against geological calibration data. *Quaternary Geochronology* 39,  
892 150-173.
- 893 Balco, G., Stone, J.O., Lifton, N.A., Dunai, T.J., 2008. A complete and easily accessible  
894 means of calculating surface exposure ages or erosion rates from  $^{10}\text{Be}$  and  $^{26}\text{Al}$   
895 measurements. *Quaternary Geochronology*, 3 (3), 174-195.
- 896 Bartz, M., 2019. Quaternary fluvial environments in NE Morocco inferred from  
897 geochronological and sedimentological investigations. *E&G Quaternary Science*  
898 *Journal* 68, 1-4.
- 899 Baynes, E.R.C., Attal, M., Niedermann, S., Kirstein, L.A., Dugmore, A.J., Naylor, M.,  
900 2015. Erosion during extreme flood events dominates Holocene canyon evolution in  
901 northeast Iceland. *Proceedings of the National Academy of Sciences*, 112 (8), 2355-  
902 2360.
- 903 Beamoud, E., Garcés, M., Montes, M., Nozal, F., Calvo, J. P., López-Olmedo, F.,  
904 Luengo, J., 2006. Magnetoestratigrafía del Mioceno de las cuencas del Tajo y del  
905 Duero. *Proceedings of the IV Simposio de Paleomagnetismo Ibérico*  
906 (MAGIBER), vol. 4, pp. 9-12.
- 907 Beaumont, C., Kooi, H., Willett, S., 2000. Coupled tectonic-surface process models  
908 with applications to rifted margins and collisional orogens. In: Summerfield, M.A.

909 (Ed.), *Geomorphology and Global Tectonics*. Chirchester, John Wiley and Sons, pp.  
910 28–55.

911 Benito-Calvo, A., Pérez-González, A., 2007. Erosion surfaces and Neogene landscape  
912 evolution in the NE Duero Basin (north-central Spain). *Geomorphology* 88, 226-241.

913 Benito-Calvo, A., Pérez-González, A. y Pares, J.M., 2008. Quantitative Reconstruction  
914 of Late Cenozoic Landscapes: A Case Study in the Sierra de Atapuerca (Burgos,  
915 Spain). *Earth Surface Processes and Landforms* 33 (2), 196-208.

916 Braucher, R., Merchel, S., Borgomano, J., Bourlès, D., 2011. Production of cosmogenic  
917 radionuclides at great depth: A multi element approach. *Earth and Planetary Science*  
918 *Letters* 309 (1-2), 1-9.

919 Bridgland, D.R., Westaway, R., 2008. Preservation patterns of Late Cenozoic fluvial  
920 deposits and their implications: Results from IGCP 449. *Quaternary International*  
921 189, 5-38.

922 Capote, R., Insua Arévalo, J.M., Martínez-Díaz, J.J., Martín-González, F., Tsige, M.,  
923 2002. La Sierra de Cártama: Pliegue con actividad reciente en las Béticas  
924 Occidentales (Hoya de Málaga). *Geogaceta* 31, 135–138.

925 Cunha, P., Martins, A.A., Huot, S., Murray, A., Raposo, L., 2008. Dating the Tejo river  
926 lower terraces in the Rodao area (Portugal) to assess the role of tectonics and uplift.  
927 *Geomorphology* 64, 271-298.

928 Cunha, P., Martins, A.A., Gomes, A., Stokes, M., Cabral, J., Lopes, F.C., Pereira, D., de  
929 Vicente, G., Builaert, J.P., Murray, A.S., Antón, L., 2019. Mechanism and age  
930 estimates of continental-scale endorheic to exorheic drainage transition: Douro  
931 River, Western Iberia. *Global and Planetary Change* 181,  
932 <https://doi.org/10.1016/j.gloplacha.2019.102985>

933 Chmeleff, J., von Blanckenburg, F., Kossert, K., Jakob, D., 2010. Determination of the  
934 <sup>10</sup>Be half-life by multicollector ICP-MS and liquid scintillation counting. *Nuclear*  
935 *Instruments and Methods in Physics Research Section B: Beam Interactions with*  
936 *Materials and Atoms*, 268 (2), 192-199.

937 Demoulin, A., Mather, A., Whittaker, A., 2017. Fluvial archives, a valuable record of  
938 vertical crustal deformation. *Quaternary Science Reviews* 166, 10-37.

939 De Vicente, G., Vegas, R., 2009. Large-scale distributed deformation controlled  
940 topography along the western Africa-Eurasia limit: Tectonic constraints.  
941 *Tectonophysics* 474 (1-2), 124-143.



942 Dunai, T.J., 2010. *Cosmogenic Nuclides: Principles, concepts and applications in the*  
943 *Earth Surface Sciences*. Cambridge University Press, 187 pp.

944 Finnegan, N.J., 2013. Interpretation and downstream correlation of bedrock river terrace  
945 treads created from propagating knickpoints. *Journal of Geophysical Research: Earth*  
946 *Surface*, 118 (1), 54-64.

947 Friend, P.F., Dabrio, C.J., 1996. *Tertiary basins of Spain: the stratigraphic record of*  
948 *crustal kinematics*. Cambridge University Press, Cambridge.

949 García-Castellanos, D., Larrasoaña, J.C., 2015. Quantifying the post-tectonic  
950 topographic evolution of closed basins: The Ebro basin (northeast Iberia). *Geology*  
951 43, 663-666.

952 García-Castellanos, D., Vergés, J., Gaspar-Escribano, J., Cloetingh, S., 2003. Interplay  
953 between tectonics, climate, and fluvial transport during the Cenozoic evolution of the  
954 Ebro Basin (NE Iberia). *Journal of Geophysical Research: Solid Earth* 108, 2347.

955 Gómez-Ortiz, D., Tejero-Lopez, R., Babín-Vich, R., Rivas-Poncé, A., 2005. Crustal  
956 density structure in the Spanish Central System derived from gravity data analysis  
957 (central Spain). *Tectonophysics* 403, 131–149.

958 González de Vallejo, L.I., 2002. *Ingeniería geológica*. Pearson Prentice Hall, 744 pp.

959 Gosse, J.C., Phillips, F., 2001. Terrestrial in situ cosmogenic nuclides: theory and  
960 application. *Quaternary Science Reviews*, 20, 1475-1560.

961 Granger, D.E., Muzikar, P.F., 2001. Dating sediment burial with in situ-produced  
962 cosmogenic nuclides: theory, techniques, and limitations. *Earth and Planetary*  
963 *Science Letters* 188, 269-281.

964 He, P., Wang, X., Song, C., Wang, Q., Deng, L., Zhong, S., 2017. Cenozoic evolution  
965 of the Western Qinling Mt. Range based on thermochronologic and sedimentary  
966 records from the Wudu Basin, NE Tibetan Plateau. *Journal of Asian Earth Sciences*  
967 138, 484-494.

968 Heidarzadeh, G., Ballato, P., Hassanzadeh, J., Ghassemi, M.R., Strecker, M.R., 2017.  
969 Lake overflow and onset of fluvial incision in the Iranian Plateau: Insights from the  
970 Mianeh Basin. *Earth and Planetary Science Letters* 469, 135-147.

971 Heisinger, B., Lal, D., Jull, A. J. T., Kubik, P., Ivy-Ochs, S., Knie, K. and Nolte, E.,  
972 2002a. Production of selected cosmogenic radionuclides by muons: 2. Capture of  
973 negative muons, *Earth and Planetary Science Letters* 200, 357–369.

974 Heisinger, B., Lal, D., Jull, A. J. T., Kubik, P., Ivy-Ochs, S., Neumaier, S., Knie, K.,  
975 Lazarev, V. and Nolte, E., 2002b. Production of selected cosmogenic radionuclides  
976 by muons 1. Fast muons, *Earth and Planetary Science Letters* 200, 345-355.

977 Krijgsman, W., Garcés, M., Langereis, C.G., Daams, R., van Dam, J., van der Meulen,  
978 A.J., Agustí, J., Cabrera, L., 1996. A new chronology for the middle to late Miocene  
979 continental record in Spain. *Earth and Planetary Science Letters* 142, 367-380.

980 Lal, D., 1991. Cosmic ray labeling of erosion surfaces: in situ nuclide production rates  
981 and erosion models. *Earth and Planetary Science Letters*, 104, 424-439.

982 Lal, D., Arnold, J.R., 1985. Tracing quartz through the environment. *Proceedings of the*  
983 *Indian Academy of Sciences-Earth and Planetary Sciences*, 94, Issue 1, pp. 1-5.

984 Mather, A.E., 2000. Adjustment of a drainage network to capture induced base-level  
985 change: an example from the Sorbas Basin, SE Spain. *Geomorphology* 34, 271-289.

986 Mather, A.E., Stokes, M., Whitfield, E., 2017. River terraces and alluvial fans: The case  
987 for an integrated Quaternary fluvial archive. *Quaternary Science Reviews* 166, 74-  
988 90.

989 Mediavilla, R.U., Dabrio, C.J., 1989. Análisis sedimentológico de los conglomerados de  
990 Tariego (Unidad 4, Neógeno de la depresión del Duero). *Studia Geologica*  
991 *Salmanticensia*, Extraordinario No. 5, 293-310.

992 Mediavilla, R., Dabrio, C.J., Martín-Serrano, A., Santisteban, J.J., 1996. Lacustrine  
993 Neogene systems of the Duero Basin: evolution and controls. In: Friend, P.F.,  
994 Dabrio, C.J. (Eds.), *Tertiary Basins of Spain: the stratigraphic record of crustal*  
995 *kinematics*. Cambridge University Press, Cambridge, pp. 228-236.

996 Moreno, D., Falguères, C., Pérez-González, A., Duval, M., Voinchet, P., Benito-Calvo,  
997 A., Ortega, A.I., Bahain, J.J., Sala, R., Carbonell, E., Bermúdez de Castro, J.M.,  
998 Arsuaga, J.L., 2012. ESR chronology of alluvial deposits in the Arlanzón valley  
999 (Atapuerca, Spain): Contemporaneity with Atapuerca Gran Dolina site. *Quaternary*  
1000 *Geochronology* 10, 418-423.

1001 Moreno, D., Benito-Calvo, A., Falguères, C., Voinchet, P., Pérez-González, A., 2016.  
1002 Preliminary Electron Spin Resonance (ESR) dating of Arlanza valley (NE Duero  
1003 Basin, Burgos, Spain). XIV Reunión Nacional de Geomorfología, abstracts volume,  
1004 Málaga, 391-398.

1005 Nishiizumi, K., 2004. Preparation of  $^{26}\text{Al}$  AMS standards. *Nuclear Instruments and*  
1006 *Methods in Physics Research Section B* 223, 388-392.

- 1007 Paola, C., Heller, P.L., Angevine, C.L. 1992. The large-scale dynamics of grain size  
1008 variation in alluvial basins, 1: Theory. *Basin Research* 4, 73–90.
- 1009 Pazzaglia, F.K. 2003. Landscape evolution models. *Developments in Quaternary*  
1010 *science* 1, 247-274.
- 1011 Pérez-González, A., 1982. El Cuaternario de la región central de la Cuenca del Duero y  
1012 sus principales rasgos geomorfológicos, I Reunión sobre la Geología de la Cuenca  
1013 del Duero. IGME, Salamanca, pp. 641-659.
- 1014 Richardson, N.J., Densmore, A.L., Seward, D., Fowler, A., Wipf, M., Ellis, M.A.,  
1015 Yong, L., Zhang, Y., 2008. Extraordinary denudation in the Sichuan Basin: Insights  
1016 from low-temperature thermochronology adjacent to the eastern margin of the  
1017 Tibetan Plateau. *Journal of Geophysical Research: Solid Earth*, 113, B04409.
- 1018 Rixhon, G., Braucher, R., Bourlès, D., Siame, L., Bovy, B., Demoulin, A., 2011.  
1019 Quaternary river incision in NE Ardennes (Belgium)–Insights from  $^{10}\text{Be}/^{26}\text{Al}$   
1020 dating of river terraces. *Quaternary Geochronology*, 6 (2), 273-284.
- 1021 Rodés, Á., Pallàs, R., Ortuño, M., García-Melendez, E., Masana, E., 2014. Combining  
1022 surface exposure dating and burial dating from paired cosmogenic depth profiles.  
1023 Example of El Límite alluvial fan in Huércal-Overa basin (SE Iberia). *Quaternary*  
1024 *Geochronology*, 19, 127-134.
- 1025 Rodés, A., Pallàs, R., Braucher, R., Moreno, X., Masana, E., Bourlès, D.L., 2011. Effect  
1026 of density uncertainties in cosmogenic  $^{10}\text{Be}$  depth-profiles: Dating a cemented  
1027 Pleistocene alluvial fan (Carboneras Fault, SE Iberia). *Quaternary Geochronology* 6,  
1028 186-194.
- 1029 Rodríguez-Rodríguez, L., Antón, L., Pallàs, R., García-Castellanos, D., Jiménez-Munt,  
1030 I., Pastor-Martín, C., 2020. A GIS method to identify flat surfaces and restore relict  
1031 fluvial long-profiles from terrace remnants gives new clues on how large basins  
1032 respond to endo-exorheic transitions (Duero Basin, Iberian Peninsula). *Earth Surface*  
1033 *Processes and Landforms* 45 (4), 1013-1027.
- 1034 Santisteban, J.I., Schulte, L., 2007. Fluvial networks of the Iberian Peninsula: a  
1035 chronological framework. *Quaternary Science Reviews* 26, 2738-2757.
- 1036 Santisteban, J.I., Alcalá, L., Mediavilla, R.M., Alberdi, M.T., Luque, L., Mazo, A.,  
1037 Miguel, I., Morales, J., Pérez, B., 1997. El Yacimiento de Tariego de Cerrato: El  
1038 inicio de la red de drenaje actual en el sector central de la Cuenca del Duero.  
1039 *Cuadernos de Geología Ibérica* 22, 431-446.

1040 Schaller, M., Ehlers, T.A., Stor, T., Torrent, J., Lobato, L., Christl, M., Vockenhuber,  
1041 C., 2016a. Spatial and temporal variations in denudation rates derived from  
1042 cosmogenic nuclides in four European fluvial terrace sequences. *Geomorphology*  
1043 274, 180-192.

1044 Schaller, M., Ehlers, T.A., Stor, T., Torrent, J., Lobato, L., Christl, M., Vockenhuber,  
1045 C., 2016b. Timing of European fluvial terrace formation and incision rates  
1046 constrained by cosmogenic nuclide dating. *Earth and Planetary Science Letters* 451,  
1047 221-231.

1048 Silva, P.G., Roquero, E., López-Recio, M., Huerta, P., Martínez-Graña, A.M., 2017.  
1049 Chronology of fluvial terrace sequences for large Atlantic rivers in the Iberian  
1050 Peninsula (Upper Tagus and Duero drainage basins, Central Spain). *Quaternary*  
1051 *Science Reviews*, 166, 188-203.

1052 Soil Survey Staff, 2015. Illustrated guide to soil taxonomy, version 2. U.S. Department  
1053 of Agriculture, Natural Resources Conservation Service, National Soil Survey  
1054 Center, Lincoln, Nebraska. USDA, 2015. Illustrated guide to soil taxonomy

1055 Spencer, J.E., Pearthree, P.A., 2001. Headward erosion versus closed-basin spillover as  
1056 alternative causes of Neogene capture of the ancestral Colorado River by the Gulf of  
1057 California. In Young, R.A., Spamer, E.E., (Eds.), *The Colorado River: Origin and*  
1058 *Evolution: Grand Canyon, Arizona*, Grand Canyon Association Monograph 12, p.  
1059 215–222.

1060 Soria-Jáuregui, Á, Jiménez-Cantizano, F., & Antón, L. (2019). Geomorphic and  
1061 tectonic implications of the endorheic to exorheic transition of the Ebro River system  
1062 in northeast Iberia. *Quaternary Research*, 91 (2), 472-492.

1063 Stokes, M., Mather, A.E., Harvey, A.M., 2002. Quantification of river-capture-induced  
1064 base-level changes and landscape development, Sorbas Basin, SE Spain. *Geological*  
1065 *Society, London, Special Publications* 191, 23-35.

1066 Stokes, M., Mather, A.E., Rodés, A., Kearsley, S., Lewin, S., 2018. Anatomy, age and  
1067 origin of an intramontane top basin surface (Sorbas Basin, Betic Cordillera, SE  
1068 Spain). *Quaternary*1 (2), 15.

1069 Stone, J., 2000. Air pressure and cosmogenic isotope production. *Journal of*  
1070 *Geophysical Research*, 105, 23753-23759.

1071 Struth, L., Garcia-Castellanos, D., Viaplana-Muzas, M., Vergés, J., 2019. Drainage  
1072 network dynamics and knickpoint evolution in the Ebro and Duero basins: From  
1073 endorheism to exorheism. *Geomorphology* 327, 554-571.

- 1074 Torrent, J., 1976. Soil development in a sequence of river terraces in northern Spain.  
1075 CATENA, 3 (1), 137-151.
- 1076 Whipple, K.X., 2001. Fluvial landscape response time: how plausible is steady-state  
1077 denudation? American Journal of Science 301 (4–5), 313–325.
- 1078 Whipple, K.X., Tucker, G.E., 1999. Dynamics of the stream power river incision model:  
1079 implications for height limits of mountain ranges, landscape response time scales and  
1080 research needs. Journal of Geophysical Research 104, 17661–17674.
- 1081 Whittaker, A.C., Boulton, S.J. 2012. Tectonic and climatic controls on knickpoint  
1082 retreat rates and landscape response times. Journal of Geophysical research 117,  
1083 F02024.
- 1084 Yu, X., Guo, Z., Fu, S., 2015. Endorheic or exorheic: differential isostatic effects of  
1085 Cenozoic sediments on the elevations of the cratonic basins around the Tibetan  
1086 Plateau. Terra Nova 27, 21-27.